NANO LETTERS

Open Access
This article is licensed under CC-BY 4.0

pubs.acs.org/NanoLett
Letter

Ab Initio Polariton Transport Dynamics with the Classical Path Approximation

Benjamin X. K. Chng, Braden M. Weight, M. Elious Mondal, and Pengfei Huo*

Cite This: https://doi.org/10.1021/acs.nanolett.6c00383

Read Online

ACCESS | Metrics & More | Article Recommendations | Supporting Information

ABSTRACT: We present an *ab initio* framework for simulating polariton transport dynamics based on the classical path approximation (CPA). The quantum dynamics of polariton transport involves simulating many electronic degrees of freedom, making a fully *ab initio* dynamics simulation computationally expensive. We demonstrate that the CPA, which removes the need for excited-state nuclear gradients, is well-suited for polaritonic systems because collective light−matter coupling leads to vanishing excited-state forces. Benchmark comparisons between CPA and full evaluation of the excited-state forces show excellent agreement for polariton transport results in model light−matter systems such as polariton group velocities and mean-squared displacements. *Ab initio* simulations of polariton transport using CPA reproduce key physical trends that are observed in experiments with BODIPY molecules. Our work establishes the CPA as a highly efficient tool for *ab initio* investigations of transport and energy flow in hybrid light−matter systems.

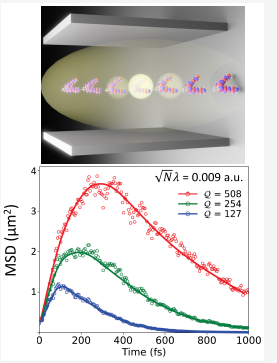

KEYWORDS: *polariton transport, ab initio on-the-fly simulations, exciton polariton, light−matter interactions, quantum electrodynamics*

Downloaded via 66.24.196.144 on April 30, 2026 at 15:05:47 (UTC).
See https://pubs.acs.org/sharingguidelines for options on how to legitimately share published articles.

Polaritons, quasi-particles formed by the hybridization of excitons and photons, have recently been shown to enhance energy transport significantly. Recent experiments have reported large group velocities for polaritons.[1−6] The exciting experimental progress in this area also sparked intensive theoretical investigations[3,7−23] on polariton transport, using both quantum dynamics simulations[3,19,24] and analytic theories.[15,17] Nonetheless, most of these investigations are limited to the simple system-bath type of exciton model systems, with a few exceptions.[9,16] On-the-fly quantum dynamics simulation is one of the most desirable approaches to explicitly describe the *ab initio* polariton nonadiabatic dynamics in realistic molecule−cavity hybrid systems. Specifically, one requires both ground- and excited-state energies and all state-to-state electric transition and permanent dipole moments, in addition to various response properties of the electronic system such as nuclear gradients of the energies, transition dipole moments, and nonadiabatic couplings,[25] all at each time step. These evaluations of these gradients make the quantum dynamics simulations in the collective coupling regime computationally prohibitive. In excited-state simulations, a widely used approximation[26−29] solves the nonadiabatic time-dependent Schrodinger equation (TDSE) on the ground-state classical trajectory. On the other hand, the quantum subsystem would still evolve based on the TDSE for the quantum subsystem. The approximation mentioned above is often termed the classical path approximation (CPA). In this paper, we investigate the validity of the CPA by simulating the quantum dynamics of the generalized Holstein−Tavis−Cummings (HTC) Hamiltonian. The dynamics with CPA show excellent agreement compared to results obtained from the full evaluation of the nonadiabatic and cavity-mediated forces. Further *ab initio* simulations of polariton transport for BODIPY molecules coupled to a FP cavity[2] are performed in this framework under CPA, and the results reproduce key experimental features, such as the polariton wavepacket's mean-squared displacement (MSD), from previous experimental work.[2] The CPA[26−28] drastically reduces the cost of the electronic structure calculations and enables large-scale, accurate quantum dynamics simulations. In this work, we theoretically demonstrate that the CPA remains valid for the polariton transport dynamics as long as the dynamics themselves are delocalized among many excitonic states.

The molecular Hamiltonian is expressed as

$$\hat{H}_n = \hat{T}_{\mathbf{R}_n} + E_g(\mathbf{R}_n)|g_n(\mathbf{R}_n)\rangle\langle g_n(\mathbf{R}_n)| + E_e(\mathbf{R}_n)|e_n(\mathbf{R}_n)\rangle\langle e_n(\mathbf{R}_n)| \quad (1)$$

where $\hat{T}_{\mathbf{R}_n}$ is the nuclear kinetic energy for molecule n and $|g_n(\mathbf{R}_n)\rangle$ and $|e_n(\mathbf{R}_n)\rangle$ are the ground state and excited states, respectively. We use the generalized Tavis−Cummings (GTC) Hamiltonian[3,30−32] to describe the collective light−matter coupling between molecules and the cavity modes, as follows

Received: January 23, 2026
Revised: April 24, 2026
Accepted: April 27, 2026

ACS Publications
© XXXX The Authors. Published by American Chemical Society

https://doi.org/10.1021/acs.nanolett.6c00383
Nano Lett. XXXX, XXX, XXX−XXX

$$\hat{H} = \sum_{n=1}^{N} \hat{H}_n + \sum_{k_\parallel} \hbar\omega_{\mathbf{k}}\left(\hat{a}_{\mathbf{k}}^{\dagger}\hat{a}_{\mathbf{k}} + \frac{1}{2}\right) + \sum_{\mathbf{k},n} \sqrt{\frac{\omega_{\mathbf{k}}}{2}}\lambda_c\, \hat{\mathbf{e}}_{\mathbf{k}}\cdot\hat{\boldsymbol{\mu}}_n(\mathbf{R}_n)(\hat{a}_{\mathbf{k}}e^{i\mathbf{k}_\parallel\mathbf{x}_n} + \hat{a}_{\mathbf{k}}^{\dagger}e^{-i\mathbf{k}_\parallel\mathbf{x}_n}) \tag{2}$$

where $\hat{\mathbf{e}}_{\mathbf{k}}$ is the field polarization direction for mode $\mathbf{k}$, $\hat{\boldsymbol{\mu}}_n(\mathbf{R}_n)$ is the dipole operator of the nth molecule, and x_n is the center of mass location of the nth molecule.[30] In addition, λ_c is the light−matter coupling strength

$$\lambda_c = \sqrt{\frac{1}{\epsilon_0 \mathcal{V}}} \tag{3}$$

where $\mathcal{V}$ is the cavity effective quantization volume and ϵ_0 is the permittivity of the materials. In this work, λ_c is treated as a parameter.

We model the FP cavity with an open direction x characterized by in-plane wavevector $\mathbf{k}_\parallel$ and one confined direction z where $\mathbf{k}_\perp$ is the wavevector of the fundamental mode confined between two cavity mirrors, perpendicular to the mirror surface. The frequency of the cavity mode is given by

$$\hbar\omega_{\mathbf{k}} = \hbar c\sqrt{k_\parallel^{\,2} + k_\perp^{\,2}} \tag{4}$$

where c is the speed of light and $\hbar\omega_c = \hbar c k_\perp$ (with $k_\parallel = 0$) is the normal incidence cavity frequency. In addition, $\hat{a}_{\mathbf{k}}^{\dagger}$ and $\hat{a}_{\mathbf{k}}$ are the photonic creation and annilaition operators for mode $\mathbf{k}$, respectively. We consider $k_\parallel$ with discrete values $k_\alpha = \frac{2\pi}{NL}\alpha$, where the mode indexes $\alpha \in \left[-\frac{\mathcal{M}-1}{2}, \ldots 0, \ldots \frac{\mathcal{M}-1}{2}\right]$, and $\mathcal{M}$ is the total number of cavity modes needed to capture the relevant energies for the hybrid system.

The transport dynamics occur in the single excitation subspace

$$|E_n(\mathbf{R})\rangle = |e_n(\mathbf{R}_n)\rangle \bigotimes_{m\neq n} |g_m(\mathbf{R}_m)\rangle \bigotimes_{k_\alpha} |0_{k_\alpha}\rangle \tag{5a}$$

$$|k_\alpha\rangle = \bigotimes_{n} |g_n(\mathbf{R})\rangle \bigotimes_{k_\parallel\neq k_\alpha} |0_{k_\parallel}\rangle \otimes |1_{k_\alpha}\rangle \tag{5b}$$

where $|E_n\rangle$ is the singly excited state for the nth molecule located at x_n and $|k_\alpha\rangle$ is the one-photon-dressed ground state with photonic momentum $\hbar k_\alpha$.

We use the $\mathcal{L}$-MFE dynamics approach[33−35] to simulate the polariton transport quantum dynamics in a lossy cavity. This approach combines Meanfield Ehrenfest (MFE) dynamics and Lindblad loss dynamics, describing the exciton-photonic degrees of freedom (DOF) quantum mechanically

$$|\psi(t)\rangle = \sum_{n=1}^{N} c_n(t)|E_n(\mathbf{R}(t))\rangle + \sum_{\alpha} c_\alpha(t)|k_\alpha\rangle \tag{6}$$

The polariton quantum dynamics is propagated with

$$i\hbar\frac{\partial}{\partial t}|\psi(t)\rangle = \hat{H}_Q(\mathbf{R})|\psi(t)\rangle \tag{7}$$

where $\hat{H}_Q = \hat{H} - \sum_n \hat{T}_{\mathbf{R}_n} \equiv \hat{H}_{pl}$ is the quantum subsystem Hamiltonian (also the adiabatic polariton Hamiltonian) that includes all DOFs except the nuclear kinetic energy, $|\psi(t)\rangle$ is represented using eq 6, and the EOM is numerically solved by using the RK4 algorithm. Cavity loss is simulated through Lindblad dynamics using a stochastic approach,[33] assuming identical loss rates Γ_c for all cavity modes k_α. We define the cavity quality factor at normal incidence ($k_\parallel = 0$) as

$$Q = \hbar\omega_c/\Gamma_c = \hbar c k_\perp/\Gamma_c \tag{8}$$

Under the mixed quantum-classical dynamics approximation, the nuclear force is

$$\mathbf{F}_n = -\nabla_n E_g(\mathbf{R}_n) - |c_n(t)|^2\nabla_n[E_e(\mathbf{R}_n) - E_g(\mathbf{R}_n)] - \sum_\alpha 2Re[c_n^*(t)c_\alpha(t)e^{-ik_\alpha x_n}]\cdot\nabla_n\langle g_n|\boldsymbol{\lambda}_{\mathbf{k}}\cdot\hat{\boldsymbol{\mu}}_n|e_n\rangle \tag{9}$$

where $\nabla_n \equiv \partial/\partial\mathbf{R}_n$ and the excitation population on molecule n is $|c_n(t)|^2$ (see eq 6). The second line of eq 9 accounts for the derivative due to the nuclear position dependence of transition dipoles $\boldsymbol{\lambda}_{\mathbf{k}}\cdot\hat{\boldsymbol{\mu}}_n(\mathbf{R}_n)$, and we have considered only the transition dipole contributions. In addition, we assume that the center of mass position of molecules is fixed during polariton transport dynamics. This is in agreement with the experimental setup because the molecules are hosted within a PMMA polymer matrix[1,2] and kept immobilized. The same type of force (eq 9) is also used in mapping-based semiclassical dynamics methods[34−43] and in the Gaussian wavepacket-based method,[44−46] and our following discussions on CPA could also be applied to those methods.

Despite the available nuclear gradients and acceleration with the machine learning models,[47] in general, it is expensive to compute these excited states' gradients, $\nabla_{\mathbf{R}_n}E_e(\mathbf{R}_n)$. In addition, for the gradient term with transition dipole $\nabla_n\langle g_n|\boldsymbol{\lambda}_{\mathbf{k}}\cdot\hat{\boldsymbol{\mu}}_n(\mathbf{R}_n)|e_n\rangle$, it is also less straightforward to evaluate, although one can take advantage of the machine learning model.[47] It is thus ideal to find approximations to avoid explicitly computing these excited states and their dipole-related derivatives.

We hypothesize that under the collective light−matter coupling and in polariton transport dynamics, the CPA is an accurate approximation, such that one does not need to compute the excited states' gradients as long as polaritons are delocalized among many molecules. This is because throughout the dynamics, the polariton wavepacket is very delocalized, such that most of the $|c_n|^2$ values are small, with $|c_n|^2 \sim 1/\mathcal{N}$, where $\mathcal{N}$ is the number of molecules transiently excited among a total of N molecules in the single excitation subspace. Under a truly collective regime for polariton transport dynamics, $|c_n|^2 \ll 1$ (for a large $\mathcal{N}$), and the excited-state force contribution in eq 9 can be ignored. For typical polariton transport experiments, the initial state often has a finite width in $k_\parallel$, meaning that the polariton will span a large spatial extent at the initial time, as well as at a later time upon propagation. This is particularly true for the narrow-band excitation used in experiments[1,3] because the narrower the polariton in k space, the more it spreads out in real space. For the broadband excitation used in ref 2, the polariton wavepacket also has a finite speed in space at the initial time (see Figure 2A).

Similarly, the term related to the dipole derivative can be ignored if $|c_n| \ll 1$, given that $|c_\alpha| \leq 1$. This means that we can replace the force in eq 9 with

$$\mathbf{F}_n \approx -\nabla_n E_g(\mathbf{R}_n(t)) \tag{10}$$

meaning CPA (eq 10) is naturally valid for polariton transport problems. The CPA version of the polariton transport EOM

https://doi.org/10.1021/acs.nanolett.6c00383
Nano Lett. XXXX, XXX, XXX−XXX

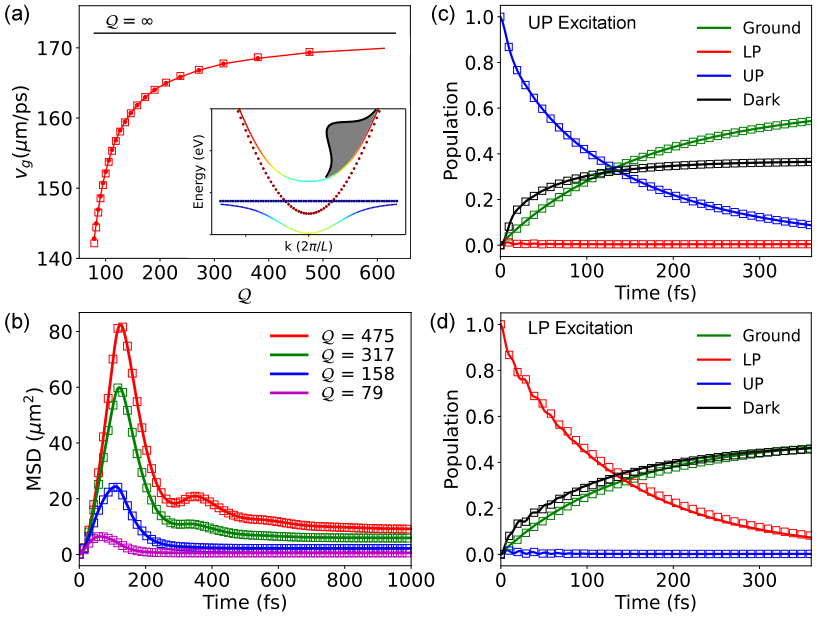

Figure 1. (a) Polariton group velocities v_g vs cavity quality factor Q for wavepackets computed with (filled circles) quantum forces on nuclei and (squares) the CPA. The inset shows the energy bandwidth used for the initial excitation in the UP branch that optimizes the localization of the polariton wavepacket. (b) Time-dependent transient MSD with UP initial excitation for different Q values. The populations of UP (blue), LP (red), dark (black), and ground states (green) in a cavity with $Q = 475$ are presented, with (c) broadband UP excitation and (d) broadband LP excitation.

thus uses eq 7 for the quantum subsystem (excitonic and photonic) and eq 10 for the update of the nuclei.

For the sake of simplicity, we have ignored the derivative coupling term $\hat{\mathbf{d}}_n = \langle g_n|\nabla_{\mathbf{R}_n}|e_n\rangle$ and Born−Oppenheimer corrections $\hat{D}_n = \langle g_n|\nabla_{\mathbf{R}_n}{}^2|e_n\rangle$ in eq 1, which will cause nonradiative relaxation from $|e_n\rangle$ to $|g_n\rangle$. These processes are less important for the ultrafast polariton transport, as the transport dynamics measured from experiments are usually shorter than the molecular exciton lifetime for the molecules.[1,2] In addition, the CPA argument can also be applied to the derivative couplings because the forces for those terms scale as $-c_i^*(t)c_j(t)[\mathbf{d}_{ij}\cdot(E_j - E_i)]$ for electronic states i and j. Note that $\mathbf{d}_{ij}$ could be large (or even singular) but $\nabla V_{ij} = [\mathbf{d}_{ij}\cdot(E_j - E_i)]$ is always finite.

We first test the validity of CPA using a system-bath model for the excitonic Hamiltonian (eq 1), allowing us to perform the simulation with the full nuclear gradients, so we can assess the validity of the CPA. The molecular Hamiltonian is

$$\hat{H}_n = \left(\hbar\omega_{ex} + \lambda_{ex} + \sum_\nu C_{n,\nu}\hat{R}_{n,\nu}\right) \otimes \hat{\sigma}_n^\dagger\hat{\sigma}_n + \sum_\nu \left(\frac{1}{2}\hat{P}_{n,\nu}{}^2 + \frac{1}{2}\omega_\nu^2\hat{R}_{n,\nu}{}^2\right) \tag{11}$$

where $\hat{\sigma}_n^\dagger = |e_n\rangle\langle g_n|$, $\hat{\sigma}_n = |g_n\rangle\langle e_n|$, $\hbar\omega_{ex}$ is the exciton energy, and $\lambda_{ex} = \sum_\nu C_{n,\nu}{}^2/\omega_\nu$ is the reorganization energy, with $C_{n,\nu}$ as the exciton−phonon coupling strength and ω_ν as the phonon frequency, and ν is the label for the phonon vibrations. In addition, $\hat{P}_{n,\nu}$ and $\hat{R}_{n,\nu}$ are the momentum and position operators, respectively, of phonon mode ν associated with exciton n. Details of the models are provided in the Supporting Information. The light−matter coupling term in eq 2 is replaced with $\sqrt{\omega_{\mathbf{k}}/2}\,\boldsymbol{\lambda}_{\mathbf{k}}\cdot\hat{\boldsymbol{\mu}}_n(\mathbf{R}_n) \to \hbar g_c\sqrt{\frac{\omega_{\mathbf{k}}}{\omega_c}}\cos\theta$ (where $\tan\theta = k_\parallel/k_\perp$), where g_c is the light−matter coupling strength in the model. Here, we use $N = 10\,001$ molecules, $\mathcal{M} = 141$ cavity modes, and reorganization energy $\lambda = 37.2$ meV. The simulation results were converged with 250 trajectories using Ehrenfest dynamics, with details provided in the Supporting Information.

Figure 1a presents the impact of varying cavity quality factor Q on v_g with a broadband excitation on the UP band (indicated with the gray Gaussian wavepacket in the inset of Figure 1a), to model experimental conditions in ref 2. The results suggest that group velocity v_g increases with increasing Q, with open circles corresponding to results using the full nuclear force expressions, and the open squares correspond to CPA results, which are in excellent agreement with the full simulation.

Figure 1b shows the transient MSD of a polariton wavepacket

$$\sigma^2(t) = \langle\psi(t)|(\hat{x} - \langle\hat{x}\rangle)^2|\psi(t)\rangle \tag{12}$$

where $\langle\hat{x}\rangle$ is the centroid of the initial polariton wavepacket (at $t = 0$) in position space (see the Supporting Information) for details. For cavities with larger Q values, both the wavepacket's maximum MSD and the corresponding rise time increase. The initial rise of MSD is due to the photonic character of the polariton wavepacket, which is responsible for ballistic transport.[8] The dip in MSD right after the initial rise is linked to both the decay of the UP population to the dark states and cavity loss, which are competing on a similar time scale.[24] The empty circles denote MSDs simulated from full calculations, and the empty squares are for MSDs computed with the CPA. As we expect, the MSDs evaluated with the two wavepackets agree well with one another.

https://doi.org/10.1021/acs.nanolett.6c00383
Nano Lett. XXXX, XXX, XXX−XXX

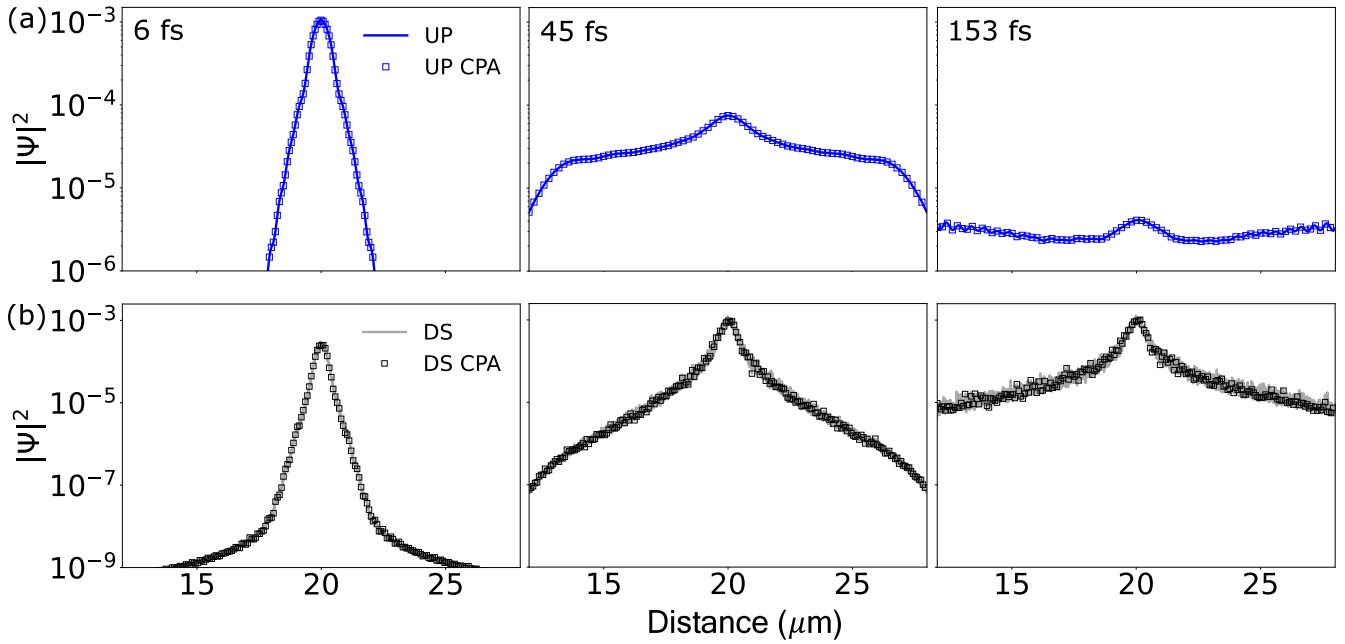

Figure 2. Wavepackets for broadband UP excitation in position space for the (a) UP wavepacket and (b) dark-state wavepacket. The simulations were performed in an FP cavity with $Q = 475$. The empty squares denote coefficients $|c_n(t)|^2$ evaluated using the CPA.

Panels c and d of Figure 1 present the population dynamics of the upper polariton (UP) (blue), lower polariton (LP) (red), and dark states (black) under broadband UP excitation and broadband LP excitation, respectively, with cavity quality factors of $Q = 475$. The ground-state population (green) is also depicted. For N molecules and $\mathcal{M}$ cavity modes, there are a total of $\mathcal{M}$ different UP and LP states each (with different k_α values) and $N - \mathcal{M}$ dark exciton states. The definitions of UP, LP, and dark states are provided in eqs S14 and S15 of the Supporting Information. In panels c and d of Figure 1, the solid lines are populations for wavepackets evaluated with the full nuclear forces while the empty squares are populations evaluated with the CPA. We see that the populations with CPA are in excellent agreement with the full calculations. We have further tested the validity of CPA with various reorganization energies λ and when considering cavity loss dynamics, with results presented in the Supporting Information.

Panels a and b of Figure 2 present the UP polariton wavepacket density and the dark exciton density in the position space for broadband UP excitations. Over time, the UP (blue) wavepacket propagates outward from the center, primarily due to its photonic character, which exhibits ballistic transport (with v_g largely adopted from the derivative of the band). Due to exciton−phonon coupling, the UP wavepackets transfer population to the dark state, resulting in an increase in the dark-state (black) probability densities. The corresponding dark-state wavepacket itself is immobile (due to the zero group velocity of the exciton band), and its spatial expansion is purely due to the expanding UP wavepacket, which deposits populations in the dark exciton states in our simulations. With the full nuclear gradient expression, we can see that the polariton wavepacket remains delocalized among a large number of $\mathcal{N}$ sites, leading to a small magnitude of the expansion coefficients of excitons ($|c_n| \ll 1$) and making the CPA a valid approximation.

We also plot the UP wavepacket and the dark-state wavepacket computed with the CPA, and they are denoted in panels a and b, respectively, of Figure 2 with empty squares. The results from CPA match closely with the full simulations. It is clear from Figure 2 that for each molecule at position x_n, the coefficients $|c_n(t)|^2 \ll 1$, satisfying the assumptions needed to use the CPA.

We further use the CPA to simulate *ab initio* polariton transport dynamics for BODIPY coupled to the cavity. The molecular ground-state energies and forces were computed using the semiempirical AM1 Hamiltonian,[48] while the excited states' energy and dipoles of these organic molecules were computed using linear-response formalism in the Tamm−Dancoff approximation (TDA-AM1), with our in-house Python code[49] interfacing with the Gaussian package.[50] Details are provided in the Supporting Information.

Figure 3 presents *ab initio* simulations of the polariton transmission spectroscopy and transport dynamics of the BODIPY molecules. The experimental investigation of the same system has been done in ref 2. Panels a and b of Figure 3 show the *ab initio* simulation of transmission polariton spectra, with $N = 108$ BODIPY molecules coupled to $\mathcal{M} = 51$ FP cavity modes for $\sqrt{N}\lambda = 0.01$ au and $\sqrt{N}\lambda = 0.02$ au, respectively. The Rabi splitting is enlarged if one increases the collective light−matter couplings. Here, we present the results as a function of the incident angle, defined as $\tan\theta = k_\parallel/k_\perp$, where $k_\parallel$ and $k_\perp$ are introduced in eq 4. The k-resolved (angle-resolved) transmission spectra are computed with

$$\mathcal{T}_J(\omega, k_\alpha) = \langle \mathcal{N}_{J,k_\alpha} \cdot \delta(\hbar\omega - \mathcal{E}_{J,k_\alpha}(\mathbf{R})) \rangle_{\mathbf{R}} \tag{13}$$

where $\mathcal{E}_{J,k_\alpha}(\mathbf{R})$ is the polariton energy for the polariton state $|\Phi_{J,k_\alpha}\rangle$ at a given k_α and $\mathcal{N}_{J,k_\alpha} = \langle \Phi_{J,k_\alpha}(\mathbf{R}) | \hat{a}_{\mathbf{k}}^\dagger \hat{a}_{\mathbf{k}} | \Phi_{J,k_\alpha}(\mathbf{R}) \rangle$ is the photon number expectation value associated with that polariton state. Computational details for the procedure are provided in the Supporting Information, with a similar computational protocol reported in our earlier work.[51]

https://doi.org/10.1021/acs.nanolett.6c00383
Nano Lett. XXXX, XXX, XXX−XXX

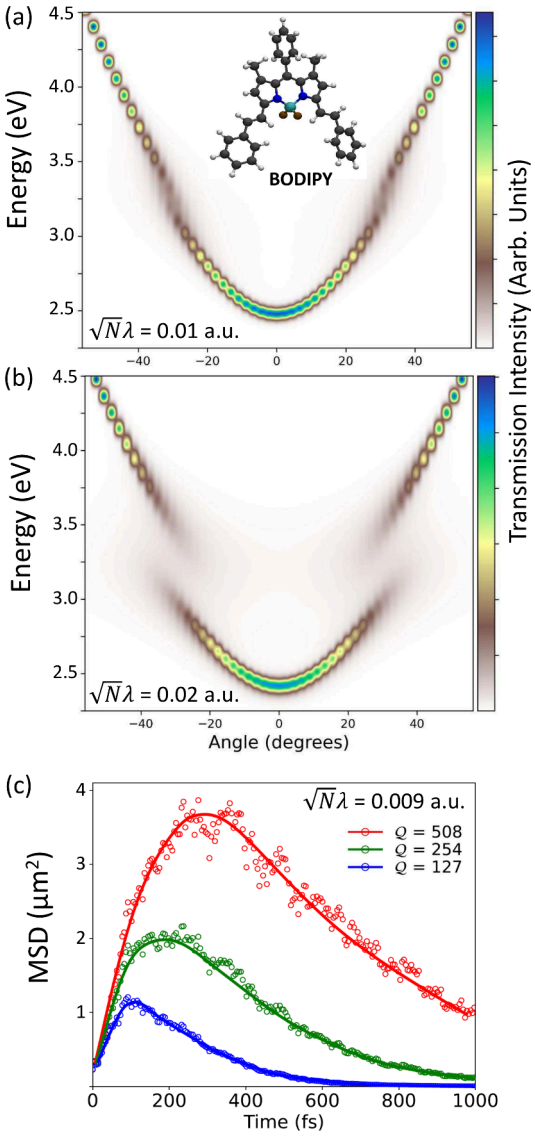

Figure 3. (a and b) Transmission spectroscopy of $N = 108$ BODIPY molecules coupled to $\mathcal{M} = 51$ cavity modes at collective light−matter coupling strength (a) $\sqrt{N}\lambda_c = 0.01$ au and (b) $\sqrt{N}\lambda_c = 0.02$ au The cavity frequency at $k_{\parallel} = 0$ is $\hbar\omega_c = 2.50$ eV. (c) Mean-squared displacement (MSD) of the polariton wavepacket over time for various cavity quality factors Q of (blue, bottom) 127, (green, middle) 254, and (red, top) 508 for initial excitation to the upper polariton. The collective light−matter coupling strength $\sqrt{N}\lambda_c \approx 0.009$ au, corresponding to $\Omega_R \approx 260$ meV under the resonant condition between light and matter with the cavity frequency at normal incidence $\hbar\omega_c = 3.0$ eV.

Figure 3c shows the *ab initio* simulation results for transient MSD, up to 1 ps, with various Q factors in the CPA framework and for a collective light−matter coupling strength that gives $\Omega_R = 260$ meV under the resonance condition. The raw data are presented with empty circles, and the thin curves provide visual guidance. We see that the time-dependent MSDs resemble those measured in the experiments (see Figure 2c of ref 2), validating our on-the-fly simulations of polariton transport dynamics with atomistic and *ab initio* details of the system. Experimentally, the MSD reported in ref 2 is based on the transient absorption measurements. The experimentally measured MSD reported in ref 2 was extracted from the transient differential transmission, and it was better connected through the following expression[8,24]

$$\sigma^2(t) = \sum_{n=1}^{N} (e^{\eta d|\psi(x_n,t)|^2} - 1) \times (x_n - \langle\hat{x}\rangle)^2 \tag{14}$$

where η is the sample's absorption coefficient, d is the optical path length, and $|\psi(x_n, t)|^2$ is the probability distribution function in site basis (see eq S23 of the Supporting Information for details). These two parameters account for the difference between the actual MSD (defined in eq 12) and the experimentally extracted MSD from the differential transmission measurements. The quantity $\exp(\eta d|\psi(x_n, t)|^2) - 1$ correlates to the transient differential transmission signal $\Delta T/T$ reported in experiments.[2,8] When $\eta d|\psi(x_n, t)|^2$ is small, which is satisfied by the polariton wavepackets, the transient differential transmission signal is approximately $\exp(\eta d|\psi(x_n, t)|^2) - 1 \approx \eta d|\psi(x_n, t)|^2$, and the transient MSD becomes $\sigma^2(t) = \eta d \sum_{n=1}^{N} |\psi(x_n, t)|^2 \times (x_n - \langle\hat{x}\rangle)^2$; this expression is identical to the simulated MSD (eq 12) with a scaling factor of ηd. We found that $\eta d = 0.0222$ reproduces the transient MSD data in ref 2. It is interesting that the *ab initio* simulation MSD behaves qualitatively similar to the HTC model presented in Figure 1b but is quantitatively different. Besides the detailed parameter differences, the realistic $E_g(\mathbf{R}_n)$ and $E_e(\mathbf{R}_n)$ are beyond the simple harmonic phonon bilinearly coupled to exciton as assumed in eq 11, and the dipole vector $\hat{\boldsymbol{\mu}}_n(\mathbf{R}_n)$ also fluctuates in time, going beyond a simple constant value. These *ab initio* atomistic features could affect the polariton dynamics. One could use machine learning approaches to build models[47] to describe these quantities and capture the effects beyond a simple model, but it takes a considerable amount of nontrivial effort.[47] CPA *ab initio* simulation, as proposed here, avoids these efforts and directly captures how $E_g(\mathbf{R}_n)$, $E_e(\mathbf{R}_n)$, and $\hat{\boldsymbol{\mu}}_n(\mathbf{R}_n)$ influence transport dynamics through eqs 2 and 6.

Figure 4 shows the transient MSD of the polariton wavepacket, up to 1 ps, with various Q factors. We show $\lambda_c = 0.0017$ au, $\lambda_c = 0.0070$ au, and $\lambda_c = 0.014$ au in panels a−c, respectively, of Figure 4, corresponding to $\Omega_R = 50$ meV, $\Omega_R = 200$ meV, and $\Omega_R = 400$ meV. The black circles in panels b and c of Figure 4 are the experimental data for ref 2 for $n = 6.5$ layers in the FP cavity. As cavity loss rate Γ_c increases, the duration of the ballistic phase, characterized by a sharp increase in the MSD, decreases, in line with previous simulations and experimental measurements. The corresponding peak MSD also decreases as Γ_c increases. In addition, we see that experimental results are in close agreement with the *ab initio* simulations for a collective light−matter coupling strength Ω_R between 200 and 400 meV and a cavity loss rate $\Gamma_c = 10$ meV (see panels b and c of Figure 4).

For more general cases in polariton photochemistry or photophysics, the condition $|c_n(t)|^2 \ll 1$ may not always be fulfilled, especially for polariton photochemistry. In polariton photochemistry,[52] it was found that the polariton state quickly localizes onto one (or a few molecules), where $|c_n|^2$ is large, and a local bond-breaking process will happen on that molecule, which does sensitively depend on the excited-state force. For polariton transport, from our results, we found that throughout

https://doi.org/10.1021/acs.nanolett.6c00383
Nano Lett. XXXX, XXX, XXX−XXX

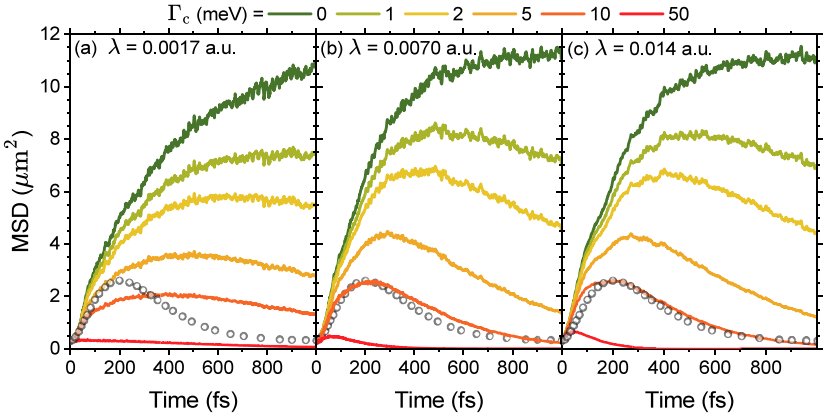

Figure 4. Mean-squared displacement (MSD) of the polariton wavepacket over time for various cavity quality factors Γ_c at collective light−matter coupling strengths (a) Ω_R = 50 meV (λ_c = 0.0017 au), (b) Ω_R = 200 meV (λ_c = 0.0070 au), and (c) Ω_R = 400 meV (λ_c = 0.014 au). Black circles are experimental data (scaled) for n = 6.5 layers in the distributed Bragg reflector (DBR) cavity in ref 2.

all t, $|c_n|^2 \ll 1$ for transport dynamics. In other words, transport dynamics could exhibit localization (due to various types of disorder). For example, when considering static exciton energy disorders, dark states are typically more localized,[11,53−55] and loss to those dark states could reintroduce localization and non-negligible excited-state force contributions. For these situations, we can instead keep tracking each $|c_n(t)|^2$ in time and start the excited-state gradient calculation only when $|c_n(t)|^2$ is larger than a certain threshold (e.g., when the force contribution is in the range of 1−5% of the ground-state force) and still keep the CPA for all other $n \neq m$. This will still drastically save a great deal of computational cost due to avoiding expensive excited-state gradients and derivative couplings. For a more detailed discussion of the CPA and the potential breakdown of it, see the Supporting Information.

In this work, we demonstrate the validity of the CPA in polariton quantum dynamics simulations. The fundamental reason why CPA works so well for polariton transport is that the polariton wavepacket remains delocalized across a large number of molecules during the dynamics, making individual expansion coefficients $|c_n(t)| \ll 1$. Thus, the excited-state contribution to the nuclear force terms, which is proportional to $|c_n|^2$, will be negligibly small compared with the ground-state forces. Neglecting the excited-state contributions in on-the-fly simulations for polariton systems in the collective coupling regime is therefore a reasonable approximation. We have tested this approximation with HTC model systems, and the results of CPA are shown to be in excellent agreement with the dynamics with full nuclear gradients. We further use CPA to perform *ab initio* polariton transport simulations with BODIPY molecules coupled to a cavity, with transient MSD results that agree well with experiments.[2] This work paves the way toward using fully *ab initio* simulations to investigate polariton transport properties in experimentally relevant systems.

■ ASSOCIATED CONTENT

Supporting Information

The Supporting Information is available free of charge at https://pubs.acs.org/doi/10.1021/acs.nanolett.6c00383.

Details of the model Hamiltonian, polariton quantum dynamics propagation method for model systems, details of the simulations of the *ab initio* polariton transmission spectra, details of the *ab initio* polariton quantum dynamics simulations, additional numerical results, and further discussions of the CPA (PDF)

■ AUTHOR INFORMATION

Corresponding Author

Pengfei Huo − *Department of Chemistry, The Institute of Optics, Hajim School of Engineering, and Center for Coherence and Quantum Optics, University of Rochester, Rochester, New York 14627, United States;* orcid.org/0000-0002-8639-9299; Email: pengfei.huo@rochester.edu

Authors

Benjamin X. K. Chng − *Department of Physics and Astronomy, University of Rochester, Rochester, New York 14627, United States;* orcid.org/0009-0001-1368-8719

Braden M. Weight − *Theoretical Division, Center for Integrated Nanotechnologies, Los Alamos National Laboratory, Los Alamos, New Mexico 87545, United States;* orcid.org/0000-0002-2441-3569

M. Elious Mondal − *Department of Chemistry, University of Rochester, Rochester, New York 14627, United States*

Complete contact information is available at: https://pubs.acs.org/10.1021/acs.nanolett.6c00383

Notes

The authors declare no competing financial interest.

■ ACKNOWLEDGMENTS

This work was supported by the Department of Energy under Grant DE-SC0026212, the University of Rochester Pump-Primer II award, and the University of Rochester Office of the Vice President for Research, the School of Medicine and Dentistry, and Arts, Sciences & Engineering via the Center for Integrated Research Computing (CIRC) through the CIRC Pilot award. B.X.K.C. appreciates the support from the Elon Huntington Hooker Fellowship from the University of Rochester. B.M.W. appreciates the support of the Director's Postdoctoral Fellowship at Los Alamos National Laboratory (LANL), which is funded by the Laboratory Directed Research and Development (LDRD) at LANL as well as the Center for Integrated Nanotechnologies (CINT) at LANL. M.E.M. appreciates the support from the Agnes M. and George Messersmith Fellowship from the University of Rochester. The

https://doi.org/10.1021/acs.nanolett.6c00383
Nano Lett. XXXX, XXX, XXX−XXX

authors appreciate the valuable comments and suggestions from Santanu Poddar. Computing resources were provided by the Center for Integrated Research Computing (CIRC) at the University of Rochester and the LANL Institutional Computing (IC) Program. P.H. appreciates valuable discussions with Andrew Musser and Milan Delor.

REFERENCES

(1) Balasubrahmaniyam, M.; Simkhovich, A.; Golombek, A.; Sandik, G.; Ankonina, G.; Schwartz, T. From enhanced diffusion to ultrafast ballistic motion of hybrid light−matter excitations. *Nat. Mater.* **2023**, *22*, 338−344.

(2) Pandya, R.; Ashoka, A.; Georgiou, K.; Sung, J.; Jayaprakash, R.; Renken, S.; Gai, L.; Shen, Z.; Rao, A.; Musser, A. J. Tuning the coherent propagation of organic exciton-polaritons through dark state delocalization. *Adv. Sci.* **2022**, *9*, 2105569.

(3) Xu, D.; Mandal, A.; Baxter, J. M.; Cheng, S.-W.; Lee, I.; Su, H.; Liu, S.; Reichman, D. R.; Delor, M. Ultrafast imaging of polariton propagation and interactions. *Nat. Commun.* **2023**, *14*, 3881.

(4) Jin, L.; Sample, A. D.; Sun, D.; Gao, Y.; Deng, S.; Li, R.; Dou, L.; Odom, T. W.; Huang, L. Enhanced two-dimensional exciton propagation via strong light−matter coupling with surface lattice plasmons. *ACS Photonics* **2023**, *10*, 1983−1991.

(5) Berghuis, A. M.; Tichauer, R. H.; de Jong, L. M.; Sokolovskii, I.; Bai, P.; Ramezani, M.; Murai, S.; Groenhof, G.; Gómez Rivas, J. Controlling exciton propagation in organic crystals through strong coupling to plasmonic nanoparticle arrays. *ACS photonics* **2022**, *9*, 2263−2272.

(6) Hong, Y.; Xu, D.; Delor, M. Exciton Delocalization Suppresses Polariton Scattering. *Chem* **2026**, *12*, 102759.

(7) Zhou, Z.; Chen, H.-T.; Sukharev, M.; Subotnik, J. E.; Nitzan, A. Nature of polariton transport in a Fabry-Perot cavity. *Phys. Rev. A* **2024**, *109*, 033717.

(8) Tichauer, R. H.; Sokolovskii, I.; Groenhof, G. Tuning the Coherent Propagation of Organic Exciton-Polaritons through the Cavity Q-factor. *Adv. Sci.* **2023**, *10*, 2302650.

(9) Sokolovskii, I.; Tichauer, R. H.; Morozov, D.; Feist, J.; Groenhof, G. Multi-scale molecular dynamics simulations of enhanced energy transfer in organic molecules under strong coupling. *Nat. Commun.* **2023**, *14*, 6613.

(10) Tutunnikov, I.; Qutubuddin, M.; Sadeghpour, H. R.; Cao, J. Characterization of Polariton Dynamics in a Multimode Cavity: Noise-enhanced Ballistic Expansion. *arXiv* **2024**, DOI: 10.48550/arXiv.2410.11051.

(11) Engelhardt, G.; Cao, J. Polariton Localization and Dispersion Properties of Disordered Quantum Emitters in Multimode Microcavities. *Phys. Rev. Lett.* **2023**, *130*, 213602.

(12) Suyabatmaz, E.; Ribeiro, R. F. Vibrational polariton transport in disordered media. *J. Chem. Phys.* **2023**, *159*, 034701.

(13) Aroeira, G. J. R.; Kairys, K. T.; Ribeiro, R. F. Coherent transient exciton transport in disordered polaritonic wires. *Nanophotonics* **2024**, *13*, 2553−2564.

(14) Krupp, N.; Groenhof, G.; Vendrell, O. Quantum Dynamics Simulation of Exciton-Polariton Transport. *Nat. Commun.* **2025**, *16*, 5431.

(15) Ying, W.; Chng, B. X.; Delor, M.; Huo, P. Microscopic theory of polariton group velocity renormalization. *Nat. Commun.* **2025**, *16*, 6950.

(16) Sokolovskii, I.; Luo, Y.; Groenhof, G. Disentangling Enhanced Diffusion and Ballistic Motion of Excitons Coupled to Bloch Surface Waves with Molecular Dynamics Simulations. *J. Phys. Chem. Lett.* **2025**, *16*, 6719−6727.

(17) Blackham, L.; Manjalingal, A.; Koshkaki, S. R.; Mandal, A. Microscopic Theory of Polaron-Polariton Dispersion and Propagation. *Nano Lett.* **2025**, *25*, 15874−15882.

(18) Manjalingal, A.; Rahmanian Koshkaki, S.; Blackham, L.; Mandal, A. Tilted Material in an Optical Cavity: Light−Matter Moiré Effect and Coherent Frequency Conversion. *ACS Photonics* **2025**, *12*, 6911−6919.

(19) Ghosh, P.; Manjalingal, A.; Wickramasinghe, S.; Koshkaki, S. R.; Mandal, A. Mean-field mixed quantum-classical approach for many-body quantum dynamics of exciton polaritons. *Phys. Rev. B* **2025**, *112*, 104319.

(20) Liu, G.; Chen, H.-T. Dissecting Exciton-Polariton Transport in Organic Molecular Crystals: Emerging Conductivity Assisted by Intermolecular Vibrational Coupling. *J. Chem. Phys.* **2025**, *163*, 174110.

(21) Fowler-Wright, P.; Reitz, M.; Yuen-Zhou, J. Mapping molecular polariton transport via pump-probe microscopy. *arXiv* **2025**, DOI: 10.48550/arXiv.2504.15501.

(22) Koshkaki, S. R.; Manjalingal, A.; Blackham, L.; Mandal, A. Exciton-Polariton Dynamics in Multilayered Materials. *arXiv* **2025**, DOI: 10.48550/arXiv.2502.12933.

(23) Poddar, S.; Huo, P. Quantum Dynamics Simulations of Polariton Transport in a Bloch Surface Wave Cavity. *ChemRxiv* **2025**, DOI: 10.26434/chemrxiv−2025−5qmxc.

(24) Chng, B. X.; Mondal, M. E.; Ying, W.; Huo, P. Quantum Dynamics Simulations of Exciton Polariton Transport. *Nano Lett.* **2025**, *25*, 1617−1622.

(25) Zhou, W.; Hu, D.; Mandal, A.; Huo, P. Nuclear gradient expressions for molecular cavity quantum electrodynamics simulations using mixed quantum-classical methods. *J. Chem. Phys.* **2022**, *157*, 104118.

(26) Akimov, A. V.; Prezhdo, O. V. The PYXAID program for non-adiabatic molecular dynamics in condensed matter systems. *J. Chem. Theory Comput.* **2013**, *9*, 4959−4972.

(27) Wang, L.; Akimov, A.; Prezhdo, O. V. Recent progress in surface hopping: 2011−2015. *journal of physical chemistry letters* **2016**, *7*, 2100−2112.

(28) Kang, J.; Wang, L.-W. Nonadiabatic molecular dynamics with decoherence and detailed balance under a density matrix ensemble formalism. *Phys. Rev. B* **2019**, *99*, 224303.

(29) Yamijala, S. S. R. K. C.; Huo, P. Direct Nonadiabatic Simulations of the Photoinduced Charge Transfer Dynamics. *J. Phys. Chem. A* **2021**, *125*, 628−635.

(30) Mandal, A.; Taylor, M. A.; Weight, B. M.; Koessler, E. R.; Li, X.; Huo, P. Theoretical advances in polariton chemistry and molecular cavity quantum electrodynamics. *Chem. Rev.* **2023**, *123*, 9786−9879.

(31) Tichauer, R. H.; Feist, J.; Groenhof, G. Multi-scale dynamics simulations of molecular polaritons: The effect of multiple cavity modes on polariton relaxation. *J. Chem. Phys.* **2021**, *154*, 104112.

(32) Taylor, M.; Mandal, A.; Huo, P. Light-Matter Interaction Hamiltonians in Cavity Quantum Electrodynamics. *ChemRxiv* **2024**, DOI: 10.26434/chemrxiv−2024−dklxd.

(33) Koessler, E. R.; Mandal, A.; Huo, P. Incorporating Lindblad decay dynamics into mixed quantum-classical simulations. *J. Chem. Phys.* **2022**, *157*, 064101.

(34) Mondal, M. E.; Koessler, E. R.; Provazza, J.; Vamivakas, A. N.; Cundiff, S. T.; Krauss, T. D.; Huo, P. Quantum dynamics simulations of the 2D spectroscopy for exciton polaritons. *J. Chem. Phys.* **2023**, *159*, 094102.

(35) Hu, D.; Chng, B. X. K.; Ying, W.; Huo, P. Trajectory-based non-adiabatic simulations of the polariton relaxation dynamics. *J. Chem. Phys.* **2025**, *162*, 124113.

(36) Lee, M. K.; Huo, P.; Coker, D. F. Semiclassical path integral dynamics: Photosynthetic energy transfer with realistic environment interactions. *Annu. Rev. Phys. Chem.* **2016**, *67*, 639−668.

(37) Bossion, D.; Ying, W.; Chowdhury, S.; Huo, P. Non-adiabatic mapping dynamics in the phase space of the SU(N) Lie group. *J. Chem. Phys.* **2022**, *157*, 084105.

(38) Weight, B. M.; Mandal, A.; Huo, P. Ab initio symmetric quasi-classical approach to investigate molecular Tully models. *J. Chem. Phys.* **2021**, *155*, 084106.

(39) Mondal, M. E.; Vamivakas, A. N.; Cundiff, S. T.; Krauss, T. D.; Huo, P. Polariton spectra under the collective coupling regime. I.

https://doi.org/10.1021/acs.nanolett.6c00383
Nano Lett. XXXX, XXX, XXX−XXX

Efficient simulation of linear spectra and quantum dynamics. *J. Chem. Phys.* **2025**, *162*, 014114.
(40) Mondal, M. E.; Vamivakas, A. N.; Cundiff, S. T.; Krauss, T. D.; Huo, P. Polariton spectra under the collective coupling regime. II. 2D non-linear spectra. *J. Chem. Phys.* **2025**, *162*, 074110.
(41) Huo, P.; Coker, D. F. Communication: Partial linearized density matrix dynamics for dissipative, non-adiabatic quantum evolution. *J. Chem. Phys.* **2011**, *135*, 201101.
(42) Weight, B. M.; Mandal, A.; Hu, D.; Huo, P. Ab initio spin-mapping non-adiabatic dynamics simulations of photochemistry. *J. Chem. Phys.* **2025**, *162*, 084105.
(43) Weight, B. M.; Sifain, A. E.; Gifford, B. J.; Htoon, H.; Tretiak, S. On-the-Fly Nonadiabatic Dynamics Simulations of Single-Walled Carbon Nanotubes with Covalent Defects. *ACS Nano* **2023**, *17*, 6208−6219.
(44) Levine, B. G.; Martínez, T. J. Isomerization Through Conical Intersections. *Annu. Rev. Phys. Chem.* **2007**, *58*, 613−634.
(45) Curchod, B. F. E.; Martínez, T. J. Ab Initio Nonadiabatic Quantum Molecular Dynamics. *Chem. Rev.* **2018**, *118*, 3305−3336.
(46) Rana, B.; Hohenstein, E. G.; Martínez, T. J. Simulating the Excited-State Dynamics of Polaritons with Ab Initio Multiple Spawning. *J. Phys. Chem. A* **2024**, *128*, 139−151.
(47) Hu, D.; Huo, P. Ab Initio Molecular Cavity Quantum Electrodynamics Simulations Using Machine Learning Models. *J. Chem. Theory Comput.* **2023**, *19*, 2353−2368.
(48) Dewar, M. J. S.; Zoebisch, E. G.; Healy, E. F.; Stewart, J. J. P. Development and use of quantum mechanical molecular models. 76. AM1: a new general purpose quantum mechanical molecular model. *J. Am. Chem. Soc.* **1985**, *107*, 3902−3909.
(49) Weight, B. M.; Mandal, A.; Huo, P. *Semiclassical Quantum Dynamics (SQD)*; 2023 (https://github.com/bradenmweight/SQD).
(50) Frisch, M. J.; Trucks, G. W.; Schlegel, H. B.; Scuseria, G. E.; Robb, M. A.; Cheeseman, J. R.; Scalmani, G.; Barone, V.; Petersson, G. A.; Nakatsuji, H.; et al. *Gaussian 16*, rev. C.01; Gaussian Inc.: Wallingford, CT, 2016.
(51) Weight, B.; Rury, A.; Shao, Y.; Huo, P. Ab Initio Polariton Spectra of ZnTPP Molecules Collectively Coupled inside an Optical Cavity. *ChemRxiv* **2025**, DOI: 10.26434/chemrxiv−2025−r98bz.
(52) Dutta, A.; Tiainen, V.; Sokolovskii, I.; Duarte, L.; Markešević, N.; Morozov, D.; Qureshi, H. A.; Pikker, S.; Groenhof, G.; Toppari, J. J. Thermal disorder prevents the suppression of ultra-fast photochemistry in the strong light-matter coupling regime. *Nat. Commun.* **2024**, *15*, 6600.
(53) Tutunnikov, I.; Qutubuddin, M.; Sadeghpour, H. R.; Cao, J. Characterization of Polariton Dynamics in a Multimode Cavity: Noise-enhanced Ballistic Expansion. *arXiv* **2024**, DOI: 10.48550/arXiv.2410.11051.
(54) Liu, T.; Yin, G.; Xiong, W. Unlocking delocalization: how much coupling strength is required to overcome energy disorder in molecular polaritons? *Chemical Science* **2025**, *16*, 4676−4683.
(55) Yin, G.; Liu, T.; Zhang, L.; Sheng, T.; Mao, H.; Xiong, W. Overcoming energy disorder for cavity-enabled energy transfer in vibrational polaritons. *Science* **2025**, *389*, 845−848.

https://doi.org/10.1021/acs.nanolett.6c00383
Nano Lett. XXXX, XXX, XXX−XXX

Supporting Information:

Ab Initio Polariton Transport Dynamics with the Classical Path Approximation

Benjamin X. K. Chng,[†] Braden M. Weight,[‡] M. Elious Mondal,[¶] and Pengfei Huo[*,¶,§,‖]

[†]*Department of Physics and Astronomy, University of Rochester, Rochester, NY 14627, U.S.A.*

[‡]*Theoretical Division, Center for Integrated Nanotechnologies, Los Alamos National Laboratory, Los Alamos, NM, 87545, U.S.A.*

[¶]*Department of Chemistry, University of Rochester, Rochester, NY 14627, U.S.A.*

[§]*The Institute of Optics, Hajim School of Engineering, University of Rochester, Rochester, NY 14627, U.S.A.*

[‖]*Center for Coherence and Quantum Optics, University of Rochester, Rochester, New York 14627, U.S.A.*

E-mail: pengfei.huo@rochester.edu

I. Model Hamiltonian Details

Generalized Holstein-Tavis-Cummings Hamiltonian.

We use the generalized Holstein-Tavis-Cummings (GHTC) Hamiltonian [1–3] to describe N molecules collectively coupled to multiple cavity modes as follows

$$\hat{H} = \hat{H}_{\text{ex}} + \hat{H}_{\text{b}} + \hat{H}_{\text{ex-b}} + \hat{H}_{\text{ph}} + \hat{H}_{\text{LM}}, \tag{S1}$$

where $\hat{H}_{\text{ex}}$ is the excitonic Hamiltonian describing N non-interacting molecules, $\hat{H}_{\text{b}}$ is the molecular bath Hamiltonian describing the phonon modes associated with each molecule, $\hat{H}_{\text{ex-b}}$ is the exciton-phonon interaction, $\hat{H}_{\text{ph}}$ is the photonic Hamiltonian describing the electromagnetic modes in a cavity, and $\hat{H}_{\text{LM}}$ is the light-matter interaction term.

The photonic Hamiltonian $\hat{H}_{\text{ph}}$ is expressed as [2–4]

$$\hat{H}_{\text{ph}} = \sum_{\text{k}_\parallel} \hbar\omega_{\mathbf{k}} (\hat{a}^\dagger_{\mathbf{k}} \hat{a}_{\mathbf{k}} + \frac{1}{2}), \tag{S2}$$

where $\mathbf{k}$ is the wave vector corresponding to a given cavity mode. Here, we analyze a one-dimensional cavity, with a quasi-continuous open direction x characterized by an in-plane wavevector $k_\parallel$, and a confined direction z where $k_\perp$ is the wavevector of the fundamental mode confined between two cavity mirrors, perpendicular to the mirror surface. Consequently, the frequencies of the cavity mode are given by

$$\hbar\omega_{\mathbf{k}} = \hbar c \sqrt{k_\parallel^2 + k_\perp^2}, \tag{S3}$$

where c is the speed of the light and we assumed the reflective index inside the cavity is $n_{\text{c}} = 1$. When $k_\parallel = 0$, $\hbar\omega_{\mathbf{k}}(0) = \hbar k_\perp = \hbar\omega_{\text{c}}$ which is the typical cavity frequency for a single-mode approximation.

Further, we assume there are N molecules equally spaced a distance L apart (lattice constant) along the $k_\parallel$ direction inside the cavity, and we assume periodic boundary conditions [2] along the $k_\parallel$ direction, such that

$$k_\alpha \equiv k_\parallel(\alpha) = \frac{2\pi}{NL}\alpha \tag{S4}$$

where the mode index is $\alpha \in [-\frac{\mathcal{M}}{2}, ...0, ...\frac{\mathcal{M}}{2}]$, and $\mathcal{M}$ is the total number of cavity modes needed to capture the relevant energies for the hybrid system.

The excitonic Hamiltonian $\hat{H}_{\text{ex}}$ is given by the expression

$$\hat{H}_{\text{ex}} = \sum_{n=0}^{N-1} (\hbar\omega_{\text{ex}} + \lambda)\hat{\sigma}_n^\dagger \hat{\sigma}_n, \tag{S5}$$

where $\hbar\omega_{\text{ex}} = E_e - E_g$ is the excitation energy between the ground and excited states, λ is the reorganization energy due to exciton-phonon coupling, defined in Eq. S12. Furthermore, $\hat{\sigma}_n^\dagger$ and $\hat{\sigma}_n$ correspond to the raising and lowering operators for the excitons (electronic degrees of freedom (DOF)). We consider a linear chain of molecules, each centered at $\mathbf{x}_n$, with a uniform spacing $L = \mathbf{x}_n - \mathbf{x}_{n-1}$, and satisfying the boundary condition $x_N = x_0$, forming a simulation box of size NL.

The light-matter interaction $\hat{H}_{\text{LM}}$ term is expressed as[1–4]

$$\hat{H}_{\text{LM}} = \sum_{\boldsymbol{k},n} \sqrt{\frac{\omega_{\boldsymbol{k}}}{2}} \boldsymbol{\lambda} \cdot \hat{\boldsymbol{\mu}}_n(\mathbf{R}_n)(\hat{a}_{\boldsymbol{k}} e^{i\boldsymbol{k}_\parallel \cdot \mathbf{x}_n} + \hat{a}_{\boldsymbol{k}}^\dagger e^{-i\boldsymbol{k}_\parallel \cdot \mathbf{x}_n}), \tag{S6}$$

where $\mathbf{x}_n = n \cdot L$ is the center of mass location of the n_{th} molecule, $\boldsymbol{\lambda}_{\boldsymbol{k}} = \sqrt{\frac{1}{\epsilon_0 V}} \hat{\mathbf{e}}_{\boldsymbol{k}}$ is the coupling for a given mode and wavevector $\boldsymbol{k}$, $\lambda = |\boldsymbol{\lambda}_{\boldsymbol{k}}|$, and $\hat{\boldsymbol{\mu}}_n(\mathbf{R}_n)$ is the dipole operator of the n_{th} molecule.[1]

In Figs. 1 and 2 in the main text, we consider the configuration of dipoles coupled to the transverse magnetic (TM) polarization (p-polarization), and Eq. S6 simplifies to

$$\hat{H}_{\text{LM}} = \sum_{k_\parallel} \sum_{n=0}^{N-1} g_{\mathbf{k}} \left(\hat{a}_{\mathbf{k}}^\dagger \hat{\sigma}_n e^{-ik_\parallel x_n} + \hat{a}_{\mathbf{k}} \hat{\sigma}_n^\dagger e^{ik_\parallel x_n} \right), \tag{S7}$$

where the $k_\parallel$-dependent light-matter coupling strength $g_{\mathbf{k}}$ in Eq. S6 is

$$g_{\mathbf{k}} = \hbar g_{\text{c}} \sqrt{\frac{\omega_{\mathbf{k}}(k_\parallel)}{\omega_{\mathbf{k}}(0)}} \cos\theta. \tag{S8}$$

In Eq. S8, g_{c} is the single-molecule coupling strength, $\tan\theta = k_\parallel / k_\perp$, and $\cos\theta = |\hat{\mu} \cdot \hat{\mathbf{e}}|$ account for the relative dipole orientation with respect to the TM field polarization. A schematic illustration can be found in Fig. S1 in Ref. 5.

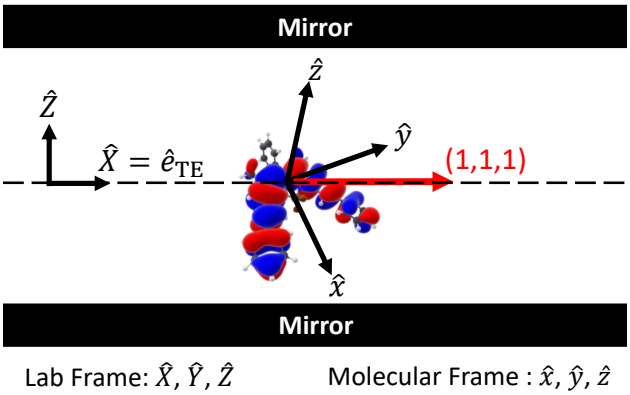

Figure S1: Schematic illustration of a BODIPY molecule inside the optical cavity. In the molecule's reference frame, denoted by $\hat{x}$, $\hat{y}$, and $\hat{z}$ unit vectors, the cavity's electric polarization points along the (1,1,1) direction. In the lab frame (cavity's frame, denoted by $\hat{X}$, $\hat{Y}$, and $\hat{Z}$ unit vectors, the cavity polarization points along the $\hat{X}$ direction. The two frames are related by a set of ordinary 3D-rotations.

For the light-matter coupling term in Eq. S6 in the *ab initio* CPA simulations (reported in Fig. 3c and Fig. 4 of the main text), we define the reference frame of a single BODIPY molecule as residing in the XY-plane. We then choose the TE cavity polarization direction, in the molecular frame, to be $\hat{\mathbf{e}}_{\mathrm{TE}} = (1,1,1)/\sqrt{3}$ for all molecules. In the cavity frame, the TE polarization points $\hat{\mathbf{e}}_{\mathrm{TE}} = \hat{X} = (1,0,0)$. These two frames are related by a set of 3D-rotations.

For the model system, each exciton is coupled to its own phonon bath modes, with the bath Hamiltonian described by

$$\hat{H}_{\mathrm{b}} = \sum_{n=0}^{N-1} \sum_{\nu} \left(\frac{1}{2} \hat{P}_{n,\nu}^2 + \frac{1}{2} \omega_{\nu}^2 \hat{R}_{n,\nu}^2 \right), \tag{S9}$$

and the system-bath (exciton-phonon) coupling term described by

$$\hat{H}_{\mathrm{sb}} = \sum_{n=0}^{N-1} \hat{\sigma}_n^{\dagger} \hat{\sigma}_n \otimes \sum_{\nu} C_{n,\nu} \hat{R}_{n,\nu}. \tag{S10}$$

Here, ω_{ν} is the frequency for the ν_{th} phonon mode, $\hat{R}_{n,\nu}$ and $\hat{P}_{n,\nu}$ are the position and momentum operators for the ν_{th} vibrational mode in the n_{th} molecule. The bath coupling constants, $c_{n,\nu}$, are

models as the Debye spectral density[6]

$$\mathcal{J}(\omega) = \frac{\pi}{2}\sum_{\nu}\frac{C_{n,\nu}^2}{\omega_{n,\nu}}\delta(\omega-\omega_{n,\nu}) = \frac{2\lambda\omega_{\rm b}\omega}{\omega_{\rm b}^2+\omega^2}, \tag{S11}$$

where λ is the reorganization energy as presented in Eq. S5, and $\omega_{\rm b}$ is the characteristic frequency of the phonon bath. Further, λ can be formally defined as

$$\lambda = \frac{2}{\pi}\int_0^\infty d\omega\frac{\mathcal{J}(\omega)}{\omega} = \sum_{\nu}\frac{C_{n,\nu}^2}{\omega_{n,\nu}^2}. \tag{S12}$$

Polaritonic States and Dark States.

The polaritonic states are defined from the GHTC Hamiltonian without the bath and exciton-phonon terms. Here, we consider the Hamiltonian $\hat{H}_{\rm pl}$ as follows

$$\hat{H}_{\rm pl} = \hat{H}_{\rm ex} + \hat{H}_{\rm ph} + \hat{H}_{\rm LM}, \tag{S13}$$

which excludes the exciton-phonon coupling $\hat{H}_{\rm ex-b}$ in the polariton Hamiltonian, as opposed to the previous work that includes them in the definition of the polariton Hamiltonian.[3,7]

We define the bright states $|{\rm B}_\alpha\rangle$ and dark states $|{\rm D}_\kappa\rangle$ of the collective matter exciton as

$$|{\rm B}_\alpha\rangle = \frac{1}{\sqrt{N}}\sum_{n=0}^{N-1}\exp\Big(-2\pi i\frac{n\alpha}{N}\Big)|E_n\rangle = \frac{1}{\sqrt{N}}\sum_{n=0}^{N-1}\exp(-ik_\alpha x_n)|E_n\rangle, \quad \alpha\in\{-\frac{\mathcal{M}}{2},\cdots,\frac{\mathcal{M}}{2}\}, \tag{S14a}$$

$$|{\rm D}_\kappa\rangle = \frac{1}{\sqrt{N}}\sum_{n=0}^{N-1}\exp\Big(-2\pi i\frac{n\kappa}{N}\Big)|E_n\rangle = \frac{1}{\sqrt{N}}\sum_{n=0}^{N-1}\exp(-ik_\kappa x_n)|E_n\rangle, \tag{S14b}$$

where the κ index for the dark states is

$$\kappa\in\left\{-\frac{N}{2},\cdots,-\left(\frac{\mathcal{M}}{2}+1\right)\right\}, \text{ and } \kappa\in\left\{\frac{\mathcal{M}}{2}+1\cdots,\frac{N}{2}\right\}, \tag{S15}$$

and there are a total of $N-\mathcal{M}$ of dark states. Further, $k_\alpha = 2\pi\alpha/(NL)$, $k_\kappa = 2\pi\kappa/(NL)$, and $x_n = nL$. The value κ does not have a matching α index, and thus, these dark states will not mix with the photonic DOF with k_α. Further, we set the indices in Eq. S14b such that the $\alpha_{\rm th}$ bright state couples to a photon mode with wave-vector k_α. Additionally, we define dark states $|{\rm D}_\kappa\rangle$ with

indices κ that are greater than $\pm\mathcal{M}/2$ (c.f. Eq. S14b).

Due to the light-matter coupling, the bright states $|\mathrm{B}_\alpha\rangle$ hybridize with the photonic states. In the current model, there are a total of $\mathcal{M}$ photonic states $\{|k_\alpha\rangle\}$ and a total of $\mathcal{M}$ bright exciton states (Eq. S14b). The hybridization of bright exciton states and photonic states generates a total of $2\mathcal{M}$ upper and lower polariton states, expressed as

$$|+, k_\alpha\rangle = \cos\Theta_N|\mathrm{B}_\alpha\rangle + \sin\Theta_N|k_\alpha\rangle, \tag{S16a}$$

$$|-, k_\alpha\rangle = -\sin\Theta_N|\mathrm{B}_\alpha\rangle + \cos\Theta_N|k_\alpha\rangle, \tag{S16b}$$

where the mixing angle Θ_N is

$$\Theta_N = \frac{1}{2}\tan^{-1}\left(\frac{2\sqrt{N}g_{\mathbf{k}}(k_\alpha)}{\omega_{\mathrm{ex}} + \lambda - \omega_{\mathbf{k}}(k_\alpha)}\right) \in [0, \frac{\pi}{2}). \tag{S17}$$

The dark states (Eq. S14) on the other hand, do not couple to the photonic DOF because there is no matching k index from the photonic DOF. These diabatic definitions of polariton and dark states will be used to interpret the quantum dynamics of the population relaxation process presented in Fig. 1 and Fig. 2 of the main text.

GHTC Model Parameters.

In simulations of the GHTC model Hamiltonian, the excitonic energy was taken to be $\hbar\omega_{\mathrm{ex}} = 1.96$ eV, and the fundamental photon frequency was taken to be $\hbar\omega_{\mathrm{c}} = 1.90$ eV (which is $\omega_{\mathbf{k}}$ at the normal incidence $k_\parallel = 0$) for the model used in Figs. 1-2 in the main text. There, $N = 10001$ molecules and $\mathcal{M} = 283$ modes were chosen, keeping the ratio of $N/\mathcal{M} \approx 35$. The inter-molecular spacing is set to be $L = 40$ Å, and the total light-matter coupling strength is fixed at $\sqrt{N}g_{\mathrm{c}} = 120$ meV.

Spacial Distribution of the Polariton Wavepacket. To interpret the spatial distribution of the polariton wavepacket at time t and position x_n, we define the time-dependent polariton state (without the ground state component)

$$|\psi(t)\rangle = \sum_{n=0}^{N-1} c_n(t)\,|E_n\rangle + \sum_\alpha c_\alpha(t)\,|k_\alpha\rangle \equiv |\psi_{\mathrm{ex}}(t)\rangle + |\psi_{\mathrm{ph}}(t)\rangle, \tag{S18}$$

and define the spatial distribution due to the excitonic part $|\psi_{\rm ex}(t)\rangle$ and photonic part $|\psi_{\rm ph}(t)\rangle$ separately. The polariton states $|\pm, n\rangle$ in real space are obtained by taking a discrete Fourier transform of Eqs. S16a and S16b using the basis $e^{ik_\alpha x_n} = e^{i\frac{2\pi\alpha}{NL}\cdot(nL)} = e^{i\frac{2\pi n\alpha}{N}}$.

This leads to the following expressions

$$|+, n\rangle = \sum_\alpha \left[\sum_{n'=0}^{N-1} \frac{X_{k_\alpha}}{N} e^{ik_\alpha(x_n - x_{n'})}|E_{n'}\rangle + C_{k_\alpha}\frac{e^{ik_\alpha x_n}}{\sqrt{N}}|k_\alpha\rangle\right], \tag{S19a}$$

$$|-, n\rangle = -\sum_\alpha \left[\sum_{n'=0}^{N-1} \frac{C_{k_\alpha}}{N} e^{ik_\alpha(x_n - x_{n'})}|E_{n'}\rangle - X_{k_\alpha}\frac{e^{ik_\alpha x_n}}{\sqrt{N}}|k_\alpha\rangle\right], \tag{S19b}$$

where $C_{k_\alpha} = \sin\Theta_N$ and $X_{k_\alpha} = \cos\Theta_N$ are the Hopfield coefficients of the polariton state with wavevector k_α. The spatial distribution of the polariton wavepacket is thus given by $|\psi_\pm(x_n, t)|^2 = |\langle\pm, n|\psi(t)\rangle|^2$, and the full expression for $|\psi_\pm(x_n, t)|^2$ is

$$\begin{aligned}|\psi_+(x_n,t)|^2 = &\left|\sum_\alpha\sum_{n'=0}^{N-1}\frac{X_{k_\alpha}}{N}e^{ik_\alpha(x_n-x_{n'})}c'_n\right|^2 + \left|\sum_\alpha C_{k_\alpha}\frac{e^{ik_\alpha x_n}}{\sqrt{N}}c_\alpha\right|^2 \\ &+ 2\mathrm{Re}\left[\sum_\alpha\sum_{n'=0}^{N-1}\frac{X_{k_\alpha}}{N}e^{ik_\alpha(x_n-x_{n'})}c'_n \times \left(\sum_{\alpha'} C_{k_{\alpha'}}\frac{e^{ik_{\alpha'}x_n}}{\sqrt{N}}c_{\alpha'}\right)^*\right],\end{aligned} \tag{S20a}$$

$$\begin{aligned}|\psi_-(x_n,t)|^2 = &\left|\sum_\alpha\sum_{n'=0}^{N-1}\frac{C_{k_\alpha}}{N}e^{ik_\alpha(x_n-x_{n'})}c'_n\right|^2 + \left|X_{k_\alpha}\frac{e^{ik_\alpha x_n}}{\sqrt{N}}c_\alpha\right|^2 \\ &- 2\mathrm{Re}\left[\sum_\alpha\sum_{n'=0}^{N-1}\frac{C_{k_\alpha}}{N}e^{ik_\alpha(x_n-x_{n'})}c'_n \times \left(\sum_{\alpha'} X_{k_{\alpha'}}\frac{e^{ik_{\alpha'}x_n}}{\sqrt{N}}c_{\alpha'}\right)^*\right].\end{aligned} \tag{S20b}$$

The last term in Eq. S20a and Eq. S20b describes the interference between the excitonic part and the photonic part of the polariton wavepacket.

The dark state wavepacket in real space is obtained by taking the discrete Fourier transform of Eq. S14, and this gives

$$|\mathrm{D}, n\rangle = \sum_\kappa \frac{1}{N}\sum_{n'=0}^{N-1} e^{ik_\kappa(x_n - x_{n'})}|E_{n'}\rangle. \tag{S21}$$

The spatial distribution of the dark state wavepacket is given by $|\psi_{\rm D}(x_n, t)|^2 = |\langle \mathrm{D}, n|\psi(t)\rangle|^2$, and is computed as

$$|\psi_{\rm D}(x_n,t)|^2 = \left|\sum_\kappa \frac{1}{N}\sum_{n'=0}^{N-1} e^{ik_\kappa(x_n-x_{n'})}c_{n'}\right|^2. \tag{S22}$$

The above polariton and dark state density dsitribuitons are used in Fig. 2 of the main text.

Transient MSD simulations. We compute the polariton group velocities and MSDs from the contributions of the polariton and dark state wavepackets

$$|\psi(x_n,t)|^2 = |\psi_+(x_n,t)|^2 + |\psi_{\rm D}(x_n,t)|^2, \tag{S23}$$

where we only count the $|+\rangle$ and dark state contribution, for the MSD reported in Fig. 1 of the main text.

The transient MSD is expressed as

$$\sigma^2(t) = \langle\psi(t)|(\hat{x} - \langle\hat{x}\rangle)^2|\psi(t)\rangle = \sum_n |\psi(x_n,t)|^2 \cdot (x_n - \langle\hat{x}\rangle)^2, \tag{S24}$$

where $\langle\hat{x}\rangle$ is the centroid of the initial polariton wavepacket (at $t = 0$) in position space. We use this expression to compute the transient MSD for the model systems (Fig. 1b in the main text).

II. Polariton Quantum Dynamics Propagation Method For Model Systems

In this work, we treat the excitonic and photonic systems as the quantum DOF, while the phonon bath as the classical DOF. By doing this, we describe the polariton dynamics associated with $\hat{H}_{\rm Q} = \hat{H} - \hat{H}_{\rm b}$ using TDSE and evolve the phonon bath DOF associated with $\hat{H}_{\rm b} + \hat{H}_{\rm ex-b}$ using Ehrenfest mean-field force. Here, we consider the single excitation subspace in our simulation. In this subspace, we consider the following matter or photonic excitations

$$|E_n\rangle = |{\rm e}_n\rangle \bigotimes_{m\neq n} |{\rm g}_m\rangle \bigotimes_{k_\parallel \in \{k_\alpha\}} |0_{k_\parallel}\rangle \tag{S25a}$$

$$|k_\alpha\rangle = |G\rangle \bigotimes_{k_\parallel \neq k_\alpha} |0_{k_\parallel}\rangle \otimes |1_{k_\alpha}\rangle\,, \tag{S25b}$$

where $|{\rm g}_n\rangle$ and $|{\rm e}_n\rangle$ represent the ground and excited states of the $n_{\rm th}$ molecule, respectively, and $|G\rangle = \bigotimes_n |g_n\rangle$ represents the matter ground state. The excitation of the $\alpha_{\rm th}$ photon mode with in-plane wave-vector k_α is given by $|1_{k_\alpha}\rangle$, while $|0_{k_\alpha}\rangle$ represents the vacuum state of the $\alpha_{\rm th}$ photonic mode.

Details of the $\mathcal{L}$-MFE approach.

To perform the transport simulations, Ehrenfest dynamics is employed, where we simulate an ensemble of trajectories with varied initial conditions. Within each trajectory, the exciton-photon wavefunction is propagated in accordance with the equation

$$-i\hbar\dot{\mathbf{c}}(t) = \hat{H}_{\mathrm{Q}}(\mathbf{R}(t))\mathbf{c}(t), \tag{S26}$$

where $\mathbf{c}(t) = [\{c_n(t)\}, \{c_\alpha(t)\}]^{\mathrm{T}}$ are the expansion coefficients, with a total of N exciton coefficients $c_n(t)$, a total of $\mathcal{M}$ photonic coefficient $c_\alpha(t)$. The nuclear coordinates are updated according to Newton's equation of motion

$$\frac{\partial R_{n,\nu}}{\partial t} = P_{n,\nu}, \quad \frac{\partial P_{n,\nu}}{\partial t} = \mathcal{F}_{n,\nu} \tag{S27}$$

where the bath modes experience the force from the potential energy surface generated by $|\psi(t)\rangle$,

$$\begin{aligned} \mathcal{F}_{n,\nu} &= -\nabla_{R_{n,\nu}} \langle\psi(t)|(\hat{H}_{\mathrm{ex-b}} + \hat{H}_{\mathrm{b}})|\psi(t)\rangle \\ &= -\omega_\nu^2 R_{n,\nu} - |c_n(t)|^2 \cdot C_{n,\nu}, \end{aligned} \tag{S28}$$

where we used the diagonal structure of bi-linear system-bath interaction in the HTC Hamiltonian (Eq. S10), and only $|E_n\rangle$ has the exciton-phonon coupling (whereas $|k_\alpha\rangle$ does not). Here, $C_{n,\nu}$ is the exciton-phonon coupling strength between phonon mode $R_{n,\nu}$ and exciton state $|E_n\rangle$, see Eq. S10. The CPA approximation corresponds to explicitly taking the $|c_n(t)|^2 \to 0$ limit, and resulting in $\mathcal{F}_{n,\nu} \approx -\omega_\nu^2 R_{n,\nu}$ for the HTC model Hamiltonian.

The cavity loss (photon loss) dynamics from state $|k_\alpha\rangle$ to state $|G\rangle$ is formally described using the Lindblad super operator $\hat{L}_\alpha = |G\rangle\langle k_\alpha|$. The dissipator $\mathcal{L}$ accounts for the cavity loss channel, causing the system to relax

$$\mathcal{L}[\hat{\rho}_{\mathrm{Q}}] = \sum_\alpha \Gamma_{\mathrm{c}} \Big(\hat{L}_\alpha \hat{\rho}_{\mathrm{Q}} \hat{L}_\alpha^\dagger - \frac{1}{2}\{\hat{L}_\alpha^\dagger \hat{L}_\alpha, \hat{\rho}_{\mathrm{Q}}\} \Big), \tag{S29}$$

which can be formally unravelled[8] as

$$c_\alpha(t + dt) = c_\alpha(t) e^{-\Gamma_{\mathrm{c}} dt}, \tag{S30}$$

and the coefficients of the ground state change by the amount

$$c_0(t+dt) = e^{i\phi}\sqrt{|c_0(t)|^2 + (1-e^{-\Gamma_\alpha dt})|c_\alpha(t)|^2}, \tag{S31}$$

where the random phase ϕ is drawn from a uniform distribution

$$\mathcal{P}(\phi) = \frac{1}{2\Delta_\phi} \quad , \quad \Delta_\phi \leq \phi \leq \Delta_\phi \tag{S32}$$

and the width of this distribution is determined by numerically solving the transcendental equation

$$\frac{\sin(\Delta_\phi)}{\Delta_\phi} = \frac{|c_0(t)|}{\sqrt{|c_0(t)|^2 + (1-e^{\Gamma_c dt})|c_\alpha(t)|^2}}. \tag{S33}$$

Details of this algorithm can be found in Ref. 8.

III. Details of Quantum Dynamics Simulations in the Model Systems.

Polaritonic Initial Conditions.

We used polariton wavepackets that are localized over the molecules but centered around a given value of k_α as the initial conditions. To generate these wavepackets, we define the polariton states $|\Phi_J\rangle$ as follows

$$\hat{H}_{\rm pl}\,|\Phi_J\rangle = \mathcal{E}_J\,|\Phi_J\rangle\,, \tag{S34}$$

where $\hat{H}_{\rm pl} = \hat{H}_{\rm ex} + \hat{H}_{\rm ph} + \hat{H}_{\rm LM}$, and the state $|\Phi_J\rangle$ has the polariton energy $\mathcal{E}_J$. Additionally, we note that the polariton states obtained from diagonalization take the form

$$|\Phi_J\rangle = \sum_n \tilde{c}_{n,J}\,|E_n\rangle + \sum_\alpha \tilde{c}_{\alpha,J}\,|k_\alpha\rangle\,, \tag{S35}$$

where $\tilde{c}_{n,J}$ and $\tilde{c}_{\alpha,J}$ are the excitonic and photonic components of the $J_{\rm th}$ polariton state, respectively.

To obtain a spatially localized polaritonic initial state, corresponding to a specific energy window $\mathcal{E} \in [\mathcal{E}_0 - \Delta\mathcal{E}/2, \mathcal{E} + \Delta\mathcal{E}/2]$ (generated from initial laser excitation), we expand the initial state in

terms of the polariton states defined in Eq. (S34) as follows

$$|\psi(0)\rangle = \sum_J a_J |\Phi_J\rangle, \tag{S36}$$

where $a_J = \langle\Phi_J|\psi(0)\rangle$ is the expansion coefficient of the initial state $|\psi(0)\rangle$ onto $|\Phi_J\rangle$, with a_J yet to be determined. For the initial excitation in the energy window $\mathcal{E} \in [\mathcal{E}_0 - \Delta\mathcal{E}/2, \mathcal{E} + \Delta\mathcal{E}/2]$, we consider those $\{|\Phi_J\rangle\}$ such that the polariton energy $\mathcal{E}_J \in [\mathcal{E}_0 - \Delta\mathcal{E}/2, \mathcal{E} + \Delta\mathcal{E}/2]$. The coefficients a_J are then generated by minimizing the spread of the wave packet Δx^2 in the excitonic space, defined as[3]

$$\Delta x^2 = \sum_n \rho_n x_n^2 - \sum_n (\rho_n x_n)^2, \tag{S37}$$

where $\rho_n = |\langle E_n|\psi(0)\rangle|^2 / \sum_m |\langle E_m|\psi(0)\rangle|^2$ is the normalized probability of occupying molecule located at x_n, and $|E_n\rangle$ is defined in Eq. S25a. In the single-excited diabatic basis, ρ_n is expressed as

$$\rho_n = \frac{|\sum_J a_J \tilde{c}_{n,J}|^2}{\sum_m |\sum_J a_J \tilde{c}_{m,J}|^2}, \tag{S38}$$

and the spread of the wavepacket Δx^2 is given by

$$\Delta x^2 = \sum_n \frac{x_n^2 |\sum_J a_J \tilde{c}_{n,J}|^2}{\sum_m |\sum_J a_J \tilde{c}_{m,J}|^2} - \left(\frac{x_n |\sum_J a_J \tilde{c}_{n,J}|^2}{\sum_m |\sum_J a_J \tilde{c}_{m,J}|^2} \right)^2. \tag{S39}$$

Eq. (S39) is used as input in the basin hopping algorithm to determine the optimal set of coefficients $\{a_J\}$ that minimizes the spread of the wavepacket. Here, we use the basin hopping algorithm[9] to determine an optimal set $\{a_J\}$ that satisfies the above condition. To streamline the computations, we note that the number of polariton states within a given energy window is significantly smaller than the total number of states in the system. Thus, we use an iterative eigenvalue algorithm, specifically the ARPACK library,[10] to isolate the relevant polariton states for the optimization task.

Nuclear Initial Conditions for the model systems.

For the model used in Figs. 1-2 in the main text, initial bath conditions were sampled from the

analytic form of the Wigner distribution for a Gaussian bath

$$[\hat{\rho}_{\mathrm{R}}]_{\mathrm{W}}(\mathbf{R},\mathbf{P}) = \prod_{n,\nu} 2\tanh\left(\frac{\beta\hbar\omega_\nu}{2}\right)\exp\left\{-\tanh\left(\frac{\beta\hbar\omega_\nu}{2}\right)\left(\frac{\omega_\nu^2 R_{n,\nu}^2}{\hbar^2}+\frac{P_{n,\nu}^2}{\hbar^2\omega_\nu^2}\right)\right\} \tag{S40}$$

which are sampled using the Gaussian random number generator based on the Box–Muller method.

$\mathcal{L}$-MFE Simulation Details.

All results are obtained with an ensemble of 250 independent trajectories. Convergence tests are performed with up to 1000 trajectories. The nuclear time step used in $\mathcal{L}$-MFE method is $\Delta t = 2.5$ fs, where during each nuclear propagation, there are 100 electronic propagation steps with a time step $dt = 0.025$ fs. The nuclear EOM in Eq. S27 is numerically integrated with the velocity Verlet algorithm (with Force expression in Eq. S27) and the TDSE (Eq. S26) is solved with the RK4 algorithm. For each electronic time step, the Stochastic Lindblad loss described in Eq. S30-Eq. S31 is applied to update the photonic coefficients in order to capture the Lindblad loss dynamics of the cavity modes.

For the $\mathcal{L}$-MFE simulations, we sample Eq. S11 by using a total of $N_\nu = 35$ bath modes (for each molecule) for various values of λ meV, and $\omega_b = 6.2$ meV. The bath parameters are sampled using the procedure outlined in Ref. 11 as follows

$$C_{n,\nu} = 2\sqrt{\lambda\frac{\tan^{-1}(\omega_{\max}\tau_\nu)}{\pi N_\nu\omega_\nu}}, \tag{S41a}$$

$$\omega_\nu = \frac{1}{\tau_\nu}\tan\left(\frac{\nu}{N_\nu}\tan^{-1}(\omega_{\max}\tau_\nu)\right), \tag{S41b}$$

where $\tau_\nu = 1/\omega_{\mathrm{b}}$, $\omega_{\max} \gg \omega_{\mathrm{b}}$ is the maximum frequency when discretizing the bath frequencies. Here, we choose $\omega_{\max} = 20\omega_{\mathrm{b}}$.

IV. Details of the ab initio electronic structure and polariton transmission spectra simulations

For the transmission spectra shown in Fig. 3a,b in the main text, we consider a single independent-mode Hamiltonian as follows

$$\hat{H}_{\mathrm{pl}}(\mathbf{R}, k_\alpha) = \sum_{n=0}^{N-1} \hat{H}_{\mathrm{el}}(\mathbf{R}_n) + \omega_{k_\alpha} \hat{a}^\dagger_{k_\alpha} \hat{a}_{k_\alpha} + \sqrt{\frac{\omega_{k_\alpha}}{2}} \boldsymbol{\lambda}_{k_\alpha} \cdot \hat{\boldsymbol{\mu}}(\mathbf{R}_n)(\hat{a}^\dagger_{k_\alpha} + \hat{a}_{k_\alpha}), \tag{S42}$$

where $\hat{H}_{\mathrm{el}}(\mathbf{R}_n) \equiv \hat{H}_n - \hat{T}_{\mathbf{R}_n}$ is the electronic Hamiltonian of molecule n [c.f. Eq. 1 of the main text] and $\boldsymbol{\lambda}_{k_\alpha} \equiv \sqrt{\frac{1}{\epsilon \mathcal{V}}} \hat{\boldsymbol{e}}_{\mathrm{TE}}$.

Solving the polaritonic eigenvalue equation (Eq. S42)

$$\hat{H}_{\mathrm{pl}}(\mathbf{R}, k_\alpha) \left| \Phi_{J,k_\alpha}(\mathbf{R}) \right\rangle = \mathcal{E}_{J,k_\alpha}(\mathbf{R}) \left| \Phi_{J,k_\alpha}(\mathbf{R}) \right\rangle, \tag{S43}$$

we obtain in mode-specific polaritonic eigenfunctions $|\Phi_{J,k_\alpha}(\mathbf{R})\rangle$ and eigenenergies $\mathcal{E}_{J,k_\alpha(\mathbf{R})}$. Here, we use the single excitation subspace, as described in Eq. 4 in the main text.

These eigenenergies and eigenstates are then used to compute the mode-specific k_α-resolved (angle-resolved) transmission spectra through the following expression

$$\mathcal{T}_J(\omega, k_\alpha) = \left\langle \mathcal{N}_{J,k_\alpha} \cdot \delta(\hbar\omega - \mathcal{E}_{J,k_\alpha}(\mathbf{R})) \right\rangle_{\mathbf{R}}. \tag{S44}$$

Here, $\mathcal{N}_{J,k_\alpha} = \langle \Phi_{J,k_\alpha}(\mathbf{R}) | \hat{a}^\dagger_{\mathbf{k}} \hat{a}_{\mathbf{k}} | \Phi_{J,k_\alpha}(\mathbf{R}) \rangle$ is the photon number expectation value associated with polariton state J. The polaritonic density of states (delta function) was weighted by the photonic character for that polariton polariton branch to give the transmission spectra. The delta function in Eq. S44 was broadened with a Gaussian of width $\sigma \approx k_{\mathrm{B}}T = 26$ meV (room temperature fluctuation). The brightest two correspond to the UP and LP branches at a given k_α away from the zero light-matter detuning region (anti-crossing region).

The ensemble average $\langle ... \rangle_{\mathbf{R}}$ represents an average over geometries sampled from the Born-Oppenheimer Molecular Dynamics simulations, with a similar computational protocol reported in our earlier work.[12] In this work, we simulated 2 ps of Born-Oppenheimer molecular dynamics for 540

BODIPY molecules at $\Delta t = 1$ fs nuclear time step in the canonical ensemble (*i.e.*, constant NVT, with T = 300 K) using Langevin dynamics, as implemented in the SQD code[13] which interfaces with the Gaussian 16 software package.[14] The molecular ground state energies and forces were computed using the semi-empirical AM1 Hamiltonian[15] while the excited states' energy and dipoles of these organic molecules were computed using linear-response formalism in the Tamm-Dancoff approximation (TDA-AM1). The dipole-filed coupling term $\hat{\boldsymbol{\mu}}(\mathbf{R}_n)\cdot\hat{\mathbf{e}}_{\mathrm{TE}}$ is then computed, using the output of $\hat{\boldsymbol{\mu}}(\mathbf{R}_n)$ in Cartesian coordinates in 3D. Discarding the first 1.0 ps for equilibration, each of the 540 BODIPY molecules contains a 1000 fs-long trajectory, including data for the electronic transition energy and electronic transition electric dipole vectors. Note that we explicitly corrected the phase of the transition dipole, which is necessary due to the arbitrary phase of the transition density as obtained by the TDA eigenvalue equation.

To compute the mode-resolved TM spectra from the linear response frequency domain (Eq. S44), the Hamiltonian for each k_α (see Eq. S42 and Eq. S43) was built with 108 molecules, and the ensemble average was performed over a total of 5000 snapshots. Note that when computing by using Eq. S42, we are assuming the single-mode limit of the original many-mode Hamiltonian (Eq. S6). It has been theoretically justified that as long as a homogeneous molecular distribution is satisfied, the eigenspectrum and linear spectra would be identical, see Eq. 10-Eq. 16 in Ref. 16.

V. Details of the ab initio polariton quantum dynamics simulations

Parameters of Ab Initio CPA Simulations. For the ab initio CPA simulations presented in Figs. 3-4 of the main text, we use $\tilde{N} = 108$ BODIPY molecules and $\mathcal{M} = 51$ cavity modes with the mode frequency obtained based on Eq. S4 The inter-molecular spacing is set to be $\tilde{L} = 1500$ Å, such that the simulation box size $\tilde{N}\tilde{L}$ is the same as for the model system. In simulations of the GHTC model Hamiltonian, the mean exciton energy from the ab initio simulation fluctuate around $E_e - E_g \approx 3.25$ eV, and the fundamental photon frequency was taken to be $\hbar\omega_{\mathrm{c}} \approx 3$ eV (which is $\omega_{\mathbf{k}}$ at the normal incidence $k_{\|} = 0$) for the transport results presented in Fig. 3C and Fig. 4 in the main text. For the transmission spectra presented in Fig. 3A-B in the main text, a different value of the cavity frequency $\hbar\omega_{\mathrm{c}} \approx 2.5$ eV was chosen, in order to clearly demonstrate the anti-crossing behavior under the strong coupling conditions as shown in Fig. 3b of the main text.

To connect with the experiments, one can estimate the inter-molecular distance of BODIPY molecules, based on the concentration as $L = 40$Å, based on the molecular concentration reported in Ref. 17. Here, for the ab initio simulation, we choose a much larger distance $\tilde{L} = sL$, where $s = 37.5$ is the scaling factor. Here, we demonstrate that as long as $\tilde{N}\tilde{L} = NL$, where $\tilde{N} = N/s$, the transport physics is preserved, given that $\Omega_{\rm R} \sim 2\sqrt{\tilde{N}}\tilde{\lambda}_{\rm c}$ is fixed. *i.e.* when choosing $\tilde{\lambda}_{\rm c} = \sqrt{s}\lambda_{\rm c}$.

This is because for the original system with intersite distance L, $k_\alpha = \frac{2\pi}{NL} \cdot \alpha$, with $\alpha \in [-N/2, N/2]$. With a scaled parameter choice,

$$\begin{aligned}\tilde{k}_\alpha &= \frac{2\pi}{\tilde{N}\tilde{L}} \cdot \alpha \quad \text{with} \quad \alpha \in \left[-\frac{\tilde{N}}{2}, ..., \frac{\tilde{N}}{2}\right] \\ &= \frac{2\pi}{\frac{N}{s} \cdot sL}\alpha \quad \text{with} \quad \alpha \in \left[-\frac{N}{2s}, ..., \frac{N}{2s}\right] \\ &= \frac{2\pi}{NL}\alpha \quad \text{with} \quad \alpha \in \frac{1}{s}\left[-\frac{N}{2}, ..., \frac{N}{2}\right]\end{aligned}$$

As such, by scaling L to $\tilde{L} = sL$, we are effectively sampling $\frac{1}{s}$-th fraction with the same Brillouin zone with $\frac{1}{s}$-th number of grid points as earlier. On the other hand, the k-grid point density does not change within the Brillouin zone $k_\alpha \in \left[-\frac{N}{2s}, ..., \frac{N}{2s}\right]$, becaue the grid point distance $\Delta k = \frac{2\pi}{\tilde{N}\tilde{L}} = \frac{2\pi}{NL}$. The only thing that is changing is the part of the Brillouin Zone (BZ) that is being considered in the simulation. By choosing $s = 37.5$, we are considering $1/s \approx 3\%$ of the full 1st BZ, which covers the range of disorerson we reported in Fig. 3b. As such, this choice captures the important part of the transport dynamics within the relevant Brillouin Zone. Further, this will not impact the light-matter coupling term in Eq. 2 of the main text. Recall that the phase factor in the coupling term is

$$e^{-ik_\alpha x_n} = \exp\left[-i\frac{2\pi}{NL} \cdot \alpha \cdot (Ln)\right] = \exp\left[-i\frac{2\pi}{\tilde{N}\tilde{L}} \cdot \alpha \cdot (\tilde{L} \cdot \frac{n}{s})\right] \tag{S45}$$

where we have fewer sites, but the phase factor remains the same. This gives fewer terms in the sum of the number of molecules $\tilde{N}$ On the other hand, our choice of $\tilde{N}$ gives a much smaller number of dark states, which is $\tilde{N} - \mathcal{M}$ that is on the same order as the number of polariton states $\mathcal{M}$. For the result presented in this work, which has an initial UP excitation and decay to dark, the transport dynamics are not significantly impacted.

Initial Polariton Condition. For the ab initio CPA simulations to compute the MSD (Fig. 3c

and Fig. 4 in the main text), the polariton initial condition was prepared on UP state, with the same numerical methods described in Eq. S36 to Eq. S39, with a center energy of UP as $\mathcal{E}_0 = 3.38$ eV, and a energy window $\Delta\mathcal{E} = 0.1$ eV.

For the classical path approximation (CPA), the nuclear trajectories for molecule n, $\mathbf{R}_n(t)$, are pre-computed using the ground state forces

$$\mathbf{F}_n = -\nabla_n E_g(\mathbf{R}_n(t)). \tag{S46}$$

These trajectories are the same data as those used for the generation of the mode-resolved transmission spectra outlined in the previous Section.

We expand exciton-photonic degrees of freedom (DOF) quantum mechanically

$$|\psi(t)\rangle = \sum_{n=1}^{N} c_n(t)\,|E_n(\mathbf{R}(t))\rangle + \sum_{\alpha} c_\alpha(t)\,|k_\alpha\rangle\,. \tag{S47}$$

The polariton quantum dynamics is propagated with

$$i\hbar\frac{\partial}{\partial t}|\psi(t)\rangle = \hat{H}_{\mathrm{Q}}(\mathbf{R}(t))|\psi(t)\rangle, \tag{S48}$$

where $|\psi(t)\rangle$ is represented using Eq. S47, $\hat{H}_{\mathrm{Q}} = \hat{H} - \sum_n \hat{T}_{\mathbf{R}_n}$ is the polariton quantum subsystem Hamiltonian including excitonic and photonic DOFs without the nuclear kinetic energy [c.f. Eq. 2 and Eq. 6 of the main text]. We use $N = 108$ molecules coupled to the cavity in order to perform the *ab initio* CPA simulation, allowing us to have five independent realizations (*ab initio* CPA trajectories) for solving Eq. S48. The details of the electronic structure are provided in the previous section. We use $\mathcal{L}$-MFE dynamics approach[8,18,19] to simulate the polariton transport quantum dynamics in a lossy cavity for the *ab initio* systems, through stochastic Lindblad dynamics using the same algorithm described in Eq. S30-Eq. S33. The EOM in Eq. S48 is numerically solved using the RK4 algorithm, with a time step $dt = 1/500$ fs.

Spacial Distribution of the Polariton Wavepacket. To obtain the spatial distribution of the polariton wavepacket at time t and position x_n for *ab initio* transport simulations, we

diagonalize $\hat{H}_{\mathrm{Q}}(\mathbf{R}(t))$ to obtain

$$\hat{H}_{\mathrm{Q}}(\mathbf{R}(t))\,|\Phi_{J,\xi}(\mathbf{R}(t)\rangle) = \mathcal{E}_{J,\xi}(\mathbf{R}(t))\,|\Phi_{J,\xi}(\mathbf{R}(t))\rangle\,, \tag{S49}$$

where $|\Phi_{J,\xi}(\mathbf{R}(t))\rangle$ and $\mathcal{E}_{J,\xi}(\mathbf{R}(t))$ are the eigenvectors and corresponding eigenenergies of the Hamiltonian. Here, we use the label ξ to denote which polaritonic state the eigenvectors correspond to, that is $\xi \in \{+, -, \mathrm{D}\}$, and the index J represents the inclusion of states in that particular polaritonic class. The spatial distribution of the polariton wavepacket is given by the projection onto the polaritonic eigenvectors, such that for the UP and LP wavepackets, we have

$$\psi_{\pm}(x_n, t) = \sum_J \langle E_n|\Phi_{J,\pm}(\mathbf{R}(t))\rangle\langle\Phi_{J,\pm}(\mathbf{R}(t))|\psi(t)\rangle, \tag{S50}$$

and for the dark states wavepacket, we have

$$\psi_{\mathrm{D}}(x_n, t) = \sum_J \langle E_n|\Phi_{J,\mathrm{D}}(\mathbf{R}(t))\rangle\langle\Phi_{J,\mathrm{D}}(\mathbf{R}(t))|\psi(t)\rangle, \tag{S51}$$

The contribution from UP and dark state are expressed as

$$|\psi(x_n, t)|^2 = |\psi_+(x_n, t)|^2 + |\psi_{\mathrm{D}}(x_n, t)|^2. \tag{S52}$$

The transient MSD is expressed as

$$\sigma^2(t) = \langle\psi(t)|(\hat{x} - \langle\hat{x}\rangle)^2|\psi(t)\rangle = \sum_n |\psi(x_n, t)|^2 \cdot (x_n - \langle\hat{x}\rangle)^2, \tag{S53}$$

where $\langle\hat{x}\rangle$ is the centroid of the initial polariton wavepacket (at $t = 0$) in position space. We use this expression to compute the transient MSD for the ab initio CPA simulation reported in Fig. 3c and 4 of the main text.

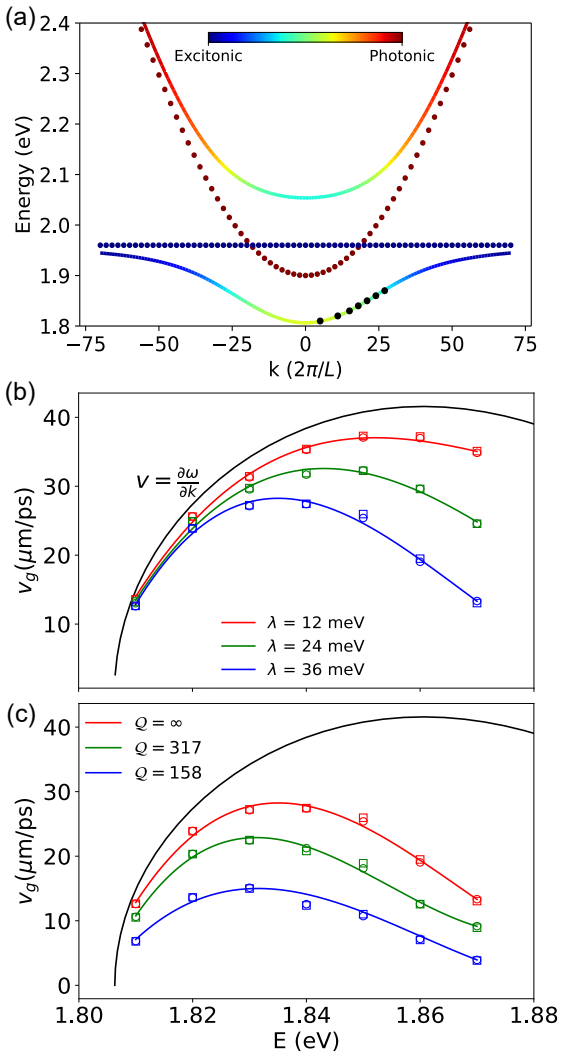

Figure S2: (a) Dispersion curve of the photon (red dots) and matter (blue dots) (b) Group velocities v_g of polaritons for various reorganization energy λ in a lossless cavity. (c) Group velocities v_g of polaritons for different cavity quality factor $\mathcal{Q}$ with phonon reorganization energy $\lambda = 36$ meV. The open circles in (b) and (c) are evaluated from wavepackets with quantum forces on the nuclei, and the open squares are evaluated from wavepackets with the CPA.

VI. Additional Numerical Results

Polariton Group Velocity Calculation with CPA using model systems

Fig. S2a presents the energy diagrams for the UP and LP bands formed from hybridizing the photonic band and the excitonic band. The LP and UP bands are color-coded based on their photonic character. The collective light-matter coupling strength is $\sqrt{N}g_c = 120$ meV. These polariton states

are analytically expressed in Eq. S16 . The initial excitation conditions are indicated in Fig. S2 using black dots on the LP branch, which corresponds to a pulse with a narrow energy bandwidth (to model the experimental condition in Ref. 3). The group velocity is extracted using the algorithm detailed in the previous work,[3,5] *e.g.*, see Eq. S60-Eq. S61 in the Supporting Information of Ref. 5.

Fig. S2b and S2c shows v_g with different initial energies (corresponding to different $k_\parallel$ in Fig. S2a). In Fig. S2b, we show results for a lossless cavity ($\Gamma_c = 0$) with varying reorganization energy, and in Fig. S2c, we show cavities with varying $\mathcal{Q}$ factor while fixing the bath parameters (λ and ω_f). The solid black line indicates the group velocity obtained as $v_g = \partial\omega_-/\partial k_\parallel$. The open circles with different colors are v_g for the excitonic system with different reorganization energy λ in Fig. S2b, and different $\mathcal{Q}$ factor in Fig. S2c. With an increase in λ, v_g decreases, which indicates that the polaritons move at a reduced v_g due to increased exciton-phonon coupling, which was previously referred to as the group velocity renormalization.[3] Similarly, decreasing $\mathcal{Q}$ causes v_g to decrease due to rapid attenuation of the photonic contribution to the polariton wavepacket. Increasing the excitonic character (increasing E) causes more renormalization of v_g, in agreement with the results in Ref. 3. The open squares with different colors are v_g computed with the CPA. We see from these results that v_g computed from wavepackets propagated using the CPA is in good agreement with v_g computed with wavepackets propagated by evaluating all contributions from the nuclear force terms.

VII. Further Discussions on CPA

The classical-path approximation (CPA),[20–22] drastically reduces the cost of the electronic structure calculations and enables large-scale, accurate quantum dynamics simulations. However, when having a small number of quantum states, CPA often faces challenges in providing accurate quantum dynamics for ab initio simulation of photochemistry[20,23] and in spin-boson model dynamics (especially at a low temperature[24,25]), due to the non-negligible nuclear forces. In this work, we theoretically demonstrate that CPA remains valid for the polariton transport dynamics, as long as the dynamics themselves are delocalized among many excitonic states. To the best of our knowledge, this is the first time that the general validity of CPA in polariton transport dynamics is theoreti-

cally investigated, as well as being used in combination with the ab initio on-the-fly simulations to investigate the transport dynamics.

Note that Ref. 26 assumes CPA and derived an analytic expression for group velocity renormalization, which agrees with the MFE simulations that do not assume CPA. This previous work provides an indirect test of the validity of CPA, and focuses only on group velocity, which does not contain the full information of transport. Here, we provide a direct test of CPA by performing the same level of simulations with the full nuclear gradient and with CPA, to directly test every possible quantum dynamical behavior of transport, including MSD, group velocity, population dynamics, and spatial-temporal polariton wavepacket. Because of these explicit and direct tests of CPA, we realized the reason behind the validity of CPA, which is that the delocalization of the wavepacket makes the approximation valid.

Theoretically, it is also possible to create a local initial excitation at just one site. We expect that the validity of CPA will break down at least for the early time dynamics when polaritons are so localized among just a few molecules. On the other hand, as the dynamics progress, the wavepacket will spread out in real space, due to the collective light-matter couplings where cavity modes are coupled to all molecular excitations (c.f. Eq. S1), and we expect that CPA will regain validity for those delocalized stages of the dynamics.

For a higher excitation subspace, such that exciton-exciton interactions become important (in the context of many-body quantum dynamics of exciton polaritons), CPA could have a higher chance to break down.[27] This is because[27] the non-adiabatic, state-dependent force $\propto N_{\rm ex} \cdot |c_n(t)|^2 \nabla_n [E_e(\mathbf{R}_n) - E_g(\mathbf{R}_n)]$, where $N_{\rm ex}$ is the number of excitons in the system,[27] which itself could be large. in Ref. 27, up to $N_{\rm ex} \sim 10^3$ was investigated. On the other hand, as long as the dynamics are delocalized, $|c_n(t)|^2 \sim 1/\mathcal{N}$, so as long as $N_{\rm ex} \ll \mathcal{N}$ in the simulation (say $\mathcal{N} \propto N \sim 10^4 - 10^6$), CPA should remain valid even for the case of transport in the higher excitation subspace. Of course, for ab initio simulations, this means that more molecules are needed when considering a large $N_{\rm ex}$. Finally, our work is limited by the accuracy of the MFE dynamics, which itself could be less accurate for non-adiabatic dynamics compared to the other available trajectory-based method.[19] The validity of CPA in MFE simulations suggests that the state-dependent nuclear forces play a negligible role in the polariton transport dynamics. Nevertheless, the CPA ground

state forces are still based on a classical approximation, and one could replace them with ground state quantum forces for the nuclei in future investigations.

References

(1) Mandal, A.; Taylor, M. A.; Weight, B. M.; Koessler, E. R.; Li, X.; Huo, P. Theoretical advances in polariton chemistry and molecular cavity quantum electrodynamics. *Chemical Reviews* **2023**, *123*, 9786–9879.

(2) Tichauer, R. H.; Feist, J.; Groenhof, G. Multi-scale dynamics simulations of molecular polaritons: The effect of multiple cavity modes on polariton relaxation. *The Journal of Chemical Physics* **2021**, *154*, 104112.

(3) Xu, D.; Mandal, A.; Baxter, J. M.; Cheng, S.-W.; Lee, I.; Su, H.; Liu, S.; Reichman, D. R.; Delor, M. Ultrafast imaging of polariton propagation and interactions. *Nature Communications* **2023**, *14*, 3881.

(4) Tichauer, R. H.; Sokolovskii, I.; Groenhof, G. Tuning the Coherent Propagation of Organic Exciton-Polaritons through the Cavity Q-factor. *Advanced Science* **2023**, *10*, 2302650.

(5) Chng, B. X.; Mondal, M. E.; Ying, W.; Huo, P. Quantum Dynamics Simulations of Exciton Polariton Transport. *Nano Letters* **2025**, *25*, 1617–1622.

(6) Nitzan, A. *Chemical dynamics in condensed phases: relaxation, transfer and reactions in condensed molecular systems*; Oxford university press, 2006.

(7) Qiu, L.; Mandal, A.; Morshed, O.; Meidenbauer, M. T.; Girten, W.; Huo, P.; Vamivakas, A. N.; Krauss, T. D. Molecular polaritons generated from strong coupling between CdSe nanoplatelets and a dielectric optical cavity. *The Journal of Physical Chemistry Letters* **2021**, *12*, 5030–5038.

(8) Koessler, E. R.; Mandal, A.; Huo, P. Incorporating Lindblad decay dynamics into mixed quantum-classical simulations. *The Journal of Chemical Physics* **2022**, *157*, 064101.

(9) Wales, D. J.; Doye, J. P. Global optimization by basin-hopping and the lowest energy structures of Lennard-Jones clusters containing up to 110 atoms. *The Journal of Physical Chemistry A* **1997**, *101*, 5111–5116.

(10) Lehoucq, R. B.; Sorensen, D. C.; Yang, C. *ARPACK users' guide: solution of large-scale eigenvalue problems with implicitly restarted Arnoldi methods*; SIAM, 1998.

(11) Huo, P.; Coker, D. F. Semi-classical path integral non-adiabatic dynamics: a partial linearized classical mapping Hamiltonian approach. *Mol. Phys.* **2012**, *110*, 1035–1052.

(12) Weight, B.; Rury, A.; Shao, Y.; Huo, P. Ab Initio Polariton Spectra of ZnTPP Molecules Collectively Coupled inside an Optical Cavity. *ChemRxiv* **2025**, 10.26434/chemrxiv–2025–r98bz.

(13) Weight, B. M.; Mandal, A.; Huo, P. Semiclassical Quantum Dynamics (SQD). 2023; `https://github.com/bradenmweight/SQD`, original-date: 2023-01-15T22:28:05Z.

(14) Frisch, M. J. et al. Gaussian˜16 Revision C.01. 2016; Gaussian Inc. Wallingford CT.

(15) Dewar, M. J. S.; Zoebisch, E. G.; Healy, E. F.; Stewart, J. J. P. Development and use of quantum mechanical molecular models. 76. AM1: a new general purpose quantum mechanical molecular model. *Journal of the American Chemical Society* **1985**, *107*, 3902–3909.

(16) Li, T. E. Vibrational polaritons with broken in-plane translational symmetry. *The Journal of Chemical Physics* **2024**, *161*, 064308.

(17) Pandya, R.; Ashoka, A.; Georgiou, K.; Sung, J.; Jayaprakash, R.; Renken, S.; Gai, L.; Shen, Z.; Rao, A.; Musser, A. J. Tuning the coherent propagation of organic exciton-polaritons through dark state delocalization. *Advanced Science* **2022**, *9*, 2105569.

(18) Mondal, M. E.; Koessler, E. R.; Provazza, J.; Vamivakas, A. N.; Cundiff, S. T.; Krauss, T. D.; Huo, P. Quantum dynamics simulations of the 2D spectroscopy for exciton polaritons. *The Journal of Chemical Physics* **2023**, *159*, 094102.

(19) Hu, D.; Chng, B. X. K.; Ying, W.; Huo, P. Trajectory-based non-adiabatic simulations of the polariton relaxation dynamics. *J. Chem. Phys.* **2025**, *162*, 124113.

(20) Akimov, A. V.; Prezhdo, O. V. The PYXAID program for non-adiabatic molecular dynamics in condensed matter systems. *Journal of chemical theory and computation* **2013**, *9*, 4959–4972.

(21) Wang, L.; Akimov, A.; Prezhdo, O. V. Recent progress in surface hopping: 2011–2015. *The journal of physical chemistry letters* **2016**, *7*, 2100–2112.

(22) Kang, J.; Wang, L.-W. Nonadiabatic molecular dynamics with decoherence and detailed balance under a density matrix ensemble formalism. *Physical Review B* **2019**, *99*, 224303.

(23) Nijjar, P.; Jankowska, J.; Prezhdo, O. V. Ehrenfest and classical path dynamics with decoherence and detailed balance. *The Journal of Chemical Physics* **2019**, *150*, 204124.

(24) Makri, N. Exploiting classical decoherence in dissipative quantum dynamics: Memory, phonon emission, and the blip sum. *Chemical Physics Letters* **2014**, *593*, 93–103.

(25) Wang, F.; Makri, N. Quantum-classical path integral with a harmonic treatment of the back-reaction. *The Journal of Chemical Physics* **2019**, *150*, 184102.

(26) Blackham, L.; Manjalingal, A.; Rahmanian Koshkaki, S.; Mandal, A. Microscopic Theory of Polaron-Polariton Dispersion and Propagation. *Nano Letters* **2025**, *25*, 15874–15882.

(27) Ghosh, P.; Manjalingal, A.; Wickramasinghe, S.; Rahmanian Koshkaki, S.; Mandal, A. Mean-field mixed quantum-classical approach for many-body quantum dynamics of exciton polaritons. *Physical Review B* **2025**, *112*, 104319.